Unifying creep and fatigue modeling of composites

A time-homogenized micromechanical framework with viscoplasticity and cohesive damage

Kovačević, D.; Hofman, P.; Rocha, I. B.C.M.; van der Meer, F. P.

DOI
10.1016/j.jmps.2024.105904

Publication date
2024

Document Version
Final published version

Published in
Journal of the Mechanics and Physics of Solids

J. Mech. Phys. Solids 193 (2024) 105904

Contents lists available at ScienceDirect

Journal of the Mechanics and Physics of Solids

journal homepage: www.elsevier.com/locate/jmps

Unifying creep and fatigue modeling of composites: A time-homogenized micromechanical framework with viscoplasticity and cohesive damage

D. Kovačević [a,b,*], P. Hofman [a], I.B.C.M. Rocha [a], F.P. van der Meer [a]

[a] Delft University of Technology, Faculty of Civil Engineering and Geosciences, PO Box 5048, 2600 GA Delft, The Netherlands
[b] DPI, PO Box 902, 5600 AX Eindhoven, The Netherlands

ARTICLE INFO

Dataset link: https://doi.org/10.4121/c9592e56-9284-42ba-92b3-b6448e5beddb

Keywords:
Fatigue
Creep
Time homogenization
Off-axis loading
Thermoplastic composites

ABSTRACT

A micromechanical model for simulating failure of unidirectional composites under cyclic loading has been developed and tested. To efficiently pass through the loading signal, a two-scale temporal framework with adaptive stepping is proposed, with a varying step size between macro time steps, and a fixed number of equally spaced micro time steps in between. With the focus on matrix dominated failure under off-axis loading, viscoplasticity and microcracking are included in the model for the polymer matrix, while carbon fibers are modeled as elastic. For a proper representation of viscous deformation in the matrix under cyclic loading, a two-scale version of the Eindhoven Glassy Polymer constitutive model is formulated, that is based on time homogenization with an effective time increment. The failure state of the representative volume element is reached by the initiation and damaging of cohesive microcracks. Cyclic and static degradation are represented by using Dávila's fatigue damage function, which is built on top of Turon's quasi-static cohesive model. The model results are compared with available experimental data on unidirectional carbon/PEEK composites tested at different stress levels, load ratios, frequencies and off-axis angles. Plasticity controlled and crack growth controlled failure mechanisms, characteristic of the long-term response of polymeric composites, are captured by the model, as well as their distinct frequency dependence. As a limit case, the model is able to reproduce the time to failure in creep loading, where the heterogeneous microstructure and viscoplastic flow of the matrix trigger the evolution of quasi-static damage. However, for the studied material system, the present model does not accurately reproduce the load ratio dependence and the off-axis angle dependence of the crack growth controlled failure mechanism.

1. Introduction

The problem of fatigue in composites sparks research effort in experimental characterization as well as in computational modeling. Experiments represent the starting point to understand the thermo-mechanical behavior of the material under different loading conditions. However, experimental campaigns for characterizing composites under fatigue loading are expensive and time consuming (Dávila, 2020). In that regard, modeling offers the possibility to reduce the number of required experiments, but also to better understand the mechanisms underlying the fatigue failure process.

* Corresponding author at: Delft University of Technology, Faculty of Civil Engineering and Geosciences, PO Box 5048, 2600 GA Delft, The Netherlands.
E-mail addresses: d.kovacevic-1@tudelft.nl (D. Kovačević), p.hofman@tudelft.nl (P. Hofman), i.rocha@tudelft.nl (I.B.C.M. Rocha), f.p.vandermeer@tudelft.nl (F.P. van der Meer).

https://doi.org/10.1016/j.jmps.2024.105904
Received 3 July 2024; Received in revised form 26 September 2024; Accepted 6 October 2024
Available online 11 October 2024

Usually two failure regimes are observed in composites under long-term loading. These two failure regimes are sometimes called plasticity controlled failure, for ductile failure, creep rupture or low-cycle fatigue, and crack growth controlled failure for brittle fracture or high-cycle fatigue (Kanters et al., 2016). When fatigue results are plotted in the form of S-t curves (maximum applied stress versus time to failure in a double logarithmic plot), the plasticity controlled regime is insensitive to the loading frequency, i.e., the material response can be approximated with a single line for different frequencies (Kanters et al., 2018). On the other hand, the time to failure in the crack growth controlled regime shows dependence on the loading frequency and shifts towards shorter timescales with increasing frequency. Alternatively, and more commonly in the composites literature, fatigue results can be reported in the form of S-N curves (maximum applied stress versus number of cycles to failure in a *loglog* plot). In this representation, the plasticity controlled mechanism is frequency-dependent, while the crack growth controlled fatigue behavior is often regarded as frequency-independent. However, frequency dependency of the crack growth mechanism was reported for glass fiber-reinforced polyphenylene-ether (PPE)/polystyrene (PS) blend by Kanters et al. (2018), depending on the load ratio R:

$$R = \frac{\sigma^{\min}}{\sigma^{\max}} \tag{1}$$

where $\sigma^{\min}$ and $\sigma^{\max}$ stand for the minimum and the maximum stress in the experiment, respectively. For lower values of the load ratio, the number of cycles to failure is largely independent of frequency (Kanters et al., 2018), and can be approximated with a single line. However, as the load ratio increases, the measured number of cycles to failure in the crack growth regime varies with frequency (Kanters et al., 2018).

The literature on micromechanical modeling of composites is rich, where representative volume elements (RVEs) with a random fiber distribution have been used to model different features of the material: stiffness (Melro et al., 2012), plastic flow (Van der Meer, 2016), strength (Totry et al., 2008), water diffusion (Rocha et al., 2017), in-situ effects (Arteiro et al., 2014), etc. However, the number of numerical models dealing with the long-term time-dependent behavior of the material, including fatigue, is limited. The majority of microscale models for fatigue are based on the mean-field homogenization techniques (Reifsnider and Gao, 1991; Hessman et al., 2023; Mohammadi et al., 2021), which are computationally efficient but miss the actual geometry of the material microstructure. In a multiscale approach, a unit cell was used by Fish and Yu (2002), and Crouch et al. (2013) to simulate the fatigue response of structural components. A model developed by Ni et al. (2023) takes into account the more detailed geometry of composites in a bond-based peridynamics framework. Although dimensionally not the microscale, an example presented in that paper closely resembles the composites microstructure loaded in transverse tension. Rocha et al. (2019) also introduced a micromechanical model for high-cycle fatigue under transverse loading together with techniques to speed-up the simulations. To the best of our knowledge, there is no computational model in the literature able to reproduce the observed frequency dependency of the S-N (or S-t) curve, for both plasticity controlled and crack growth controlled regimes. We aim to develop a model that can capture these dependencies, believing that such ability indicates that the model describes the relevant physics for time- and cycle-dependent failure of thermoplastic composites. Here, we tackle this issue by introducing a microscale spatial and two-scale temporal framework to predict failure of unidirectional (UD) composites under cyclic loading.

To impose an off-axis stress on the RVE, kinematical and stress relations inherit the form from our previously published RVE model for creep rupture (Kovačević et al., 2024). Two important requirements are set for numerical models describing the long-term behavior under cyclic loading. Firstly, the loading strategy must ensure computational feasibility, where tracing the loading path in detail is too demanding, and secondly, the material models must be formulated such that deformation of the constituents under the simplified loading strategy matches the deformation obtained for the actual loading scheme. Accordingly, we propose an adaptive two-scale time stepping scheme with time homogenization including the macro time steps where viscoplasticity evolves in the polymer matrix, and micro time steps where the material response is elastic, but the stress evolution over the cycle is recorded. The polymer response under cyclic loading is represented with the Eindhoven Glassy Polymer (EGP) material model (Van Breemen et al., 2011) for which a two-scale temporal version is formulated. The state variables of the two-scale EGP model are updated at macro time steps using an effective time increment, based on information collected at micro time steps. Carbon fibers are modeled with a hyperelastic transversely isotropic constitutive model (Bonet and Burton, 1998). Microcracking of the matrix due to cyclic loading is accounted for by means of Dávila's cycle-dependent cohesive model (Dávila, 2020), with the fatigue damage function as presented in Joosten et al. (2022). Cohesive segments are added on the fly (Camacho and Ortiz, 1996), when a suitable initiation criterion is satisfied (Hofman et al., 2024), for which we introduce a small modification in this study. The cohesive model is able to represent the kink point in S-N curve distinguishing between the low- and high-cycle failure mechanisms, but not the frequency dependency of each failure mechanism. Its formulation is built on the notion that for a given stress, the number of cycles governs failure, and includes no frequency or time dependence. The timescale, and correspondingly the observed frequency dependency, is introduced in the model through the viscous response of the matrix represented with the (two-scale) EGP model. To make the cohesive zone model compatible with the two-scale EGP model, cohesive initiation and damage evolution are blocked at micro time steps. The RVE model results are compared with available experimental S-N (or S-t) curves of UD carbon/PEEK thermoplastic composite material, tested at different load ratios, frequencies and loading angles (Sundararajan, 2024).

The content of the paper includes the following topics: homogenized kinematical and stress relations to impose an off-axis stress on the RVE; description of the bulk material models including the formulation of the two-scale EGP model; review of the cohesive zone model (CZM); introduction of the adaptive time stepping strategy; evaluation of the model performance in comparison with experimental results and conclusions.

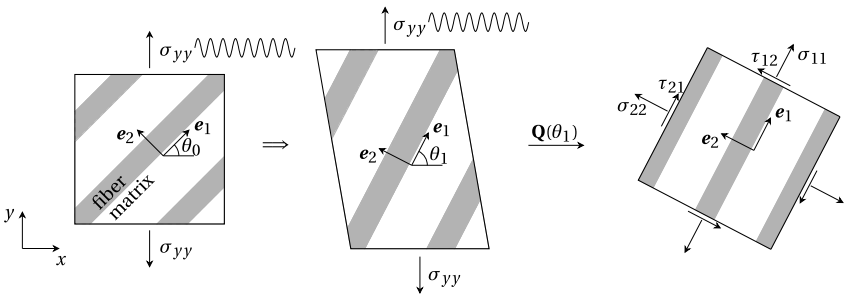

Fig. 1. Cyclic stress applied on unidirectional composite material under off-axis angle (left); deformed material (middle); Cauchy stress components on the material in local frame (right).

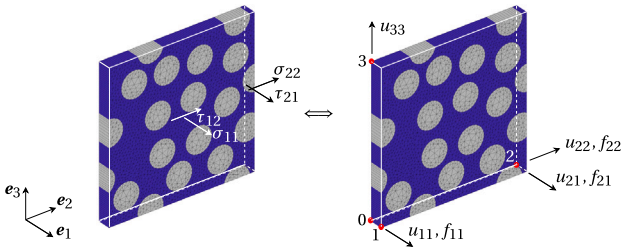

Fig. 2. Homogenized Cauchy stresses on RVE faces (left) as a result of the force vector components applied on the master nodes (right); nonzero displacements of master nodes also indicated in the right figure.

2. Off-axis loading: homogenized kinematics and stress

Uniaxial cyclic loading is applied on a unidirectional composite material under an off-axis angle, see Fig. 1 (left), where the initial off-axis angle χ is defined as: $\chi = 90° - \theta_0$, θ_0 being the initial angle between the global x-direction and the local e_1-direction. In this setting, the orthotropic material deforms in extension as well as in shear, see Fig. 1 (middle). Allowing for finite strains in the material, the local coordinate frame aligned with the reinforcement may change orientation from the angle θ_0 to a new angle θ_1. In this deformed configuration, the stress state can be transformed from the global coordinate system to the local frame, to obtain the Cauchy stress components shown in Fig. 1 (right). The goal is to simulate this deformation process on the microscale by means of a thin slice 3D RVE, aligned with the local frame. The homogenized deformation and stress state of the RVE must be the same as that in Fig. 1. Correspondingly, the homogenized Cauchy stress components acting on the RVE faces are shown in Fig. 2 (left). This stress state is imposed on the RVE with periodic boundary conditions through the force vector components applied on the four master nodes of the RVE, see Fig. 2 (right). In the same figure, along with the force vector components, the corresponding nonzero displacements of the master nodes are also indicated. A detailed discussion on this choice of boundary conditions is part of Kovačević and Van der Meer (2022). The boundary conditions enforce periodicity in the deformation process (Van der Meer, 2016), also allowing for microcracking (Ke and Van der Meer, 2022).

Equations needed to impose an off-axis loading on the RVE assuming finite deformations were introduced in Kovačević and Van der Meer (2022). A small adjustment to impose an off-axis creep stress, including a constant engineering stress, was presented in Kovačević et al. (2024). Exactly the same framework is used here, with the adjustment that the applied stress σ_{yy} cyclically changes its magnitude. Relevant equations are repeated here, without detailed explanation. Expressions for the nonzero force vector components on the master nodes read:

$$
\begin{aligned}
f_{11} &= \sigma_{yy} A_1^0 \bar{J} \left(\frac{s_1^2}{\bar{F}_{11}} - c_1 s_1 \frac{\bar{F}_{12}}{\bar{F}_{11}\bar{F}_{22}} \right) \\
f_{21} &= \sigma_{yy} A_2^0 \bar{J} \frac{c_1 s_1}{\bar{F}_{22}} \\
f_{22} &= \sigma_{yy} A_2^0 \bar{J} \frac{c_1^2}{\bar{F}_{22}}
\end{aligned}
\tag{2}
$$

where A_i^0 is the initial surface on which the corresponding stress component is acting, $\bar{J}$ is the determinant of the RVE homogenized deformation gradient in local frame $\bar{\mathbf{F}}$, s_1 and c_1 are $\sin(\theta_1)$ and $\cos(\theta_1)$ respectively, while $\bar{F}_{ij}$ are components of $\bar{\mathbf{F}}$:

$$\bar{\mathbf{F}} = \begin{bmatrix} \bar{F}_{11} & \bar{F}_{12} & 0 \\ 0 & \bar{F}_{22} & 0 \\ 0 & 0 & \bar{F}_{33} \end{bmatrix} = \begin{bmatrix} 1 + \frac{u_{11}}{l_1^0} & \frac{u_{21}}{l_2^0} & 0 \\ 0 & 1 + \frac{u_{22}}{l_2^0} & 0 \\ 0 & 0 & 1 + \frac{u_{33}}{l_3^0} \end{bmatrix} \tag{3}$$

Here, u_{ij} is the displacement of master node i in direction j, whereas l_i^0 is the initial length of the RVE in direction i. $\bar{\mathbf{F}}$ can be related to the homogenized deformation gradient in global frame $\mathbf{F}$ through the following relation:

$$\mathbf{F} = \mathbf{Q}_1^{\mathrm{T}} \bar{\mathbf{F}} \mathbf{Q}_0 \tag{4}$$

where $\mathbf{Q}_0$ is the transformation matrix:

$$\mathbf{Q}_0 = \begin{bmatrix} \cos(\theta_0) & \sin(\theta_0) & 0 \\ -\sin(\theta_0) & \cos(\theta_0) & 0 \\ 0 & 0 & 1 \end{bmatrix} \tag{5}$$

The transformation matrix $\mathbf{Q}_1$ shares the same form with $\mathbf{Q}_0$, but depends on the angle θ_1. This angle is computed as: $\theta_1 = \theta_0 + \phi$, where the angle ϕ measures reorientation of the RVE in the deformation process. The procedure to compute the angle ϕ is detailed in Kovačević and Van der Meer (2022).

By knowing $\mathbf{F}$, different strain measures in the global loading direction can be computed. For example, the true (logarithmic) strain reads:

$$\varepsilon_{yy} = \ln(F_{yy}) \tag{6}$$

where F_{yy} is a component of $\mathbf{F}$. Alternatively, the engineering strain can be computed as:

$$\varepsilon_{yy}^{\mathrm{eng}} = F_{yy} - 1 \tag{7}$$

If a constant engineering stress is considered in the analysis, the actual stress σ_{yy} in Eq. (2) is obtained by correcting the engineering stress for the previous deformation:

$$\sigma_{yy} = \frac{\sigma_{yy}^{\mathrm{eng}}}{F_{xx} F_{zz}} \tag{8}$$

where F_{xx} and F_{zz} are components of $\mathbf{F}$.

The expression for the internal force vector in the presence of cohesive microcracks and the absence of body forces is adopted according to Kovačević et al. (2022).

3. Constitutive models

In this section, the different constitutive models used in this study are described. The material parameter values that are used in the numerical simulations are also given. In the Appendix, an overview of all model parameters is given, along with a discussion on how they can be identified from experiments.

3.1. Eindhoven Glassy polymer constitutive model

To represent the behavior of the polymer matrix under cyclic loading we formulate a two-scale temporal version of the EGP material model. The governing equations of the EGP model are briefly reviewed, in order to set the stage for the two-scale version of the model.

Different from many material models dealing with plasticity, the EGP does not define a yield surface. Instead it features a viscosity function, which changes with the stress applied on the material (Tervoort et al., 1997), such that the yielding is considered as the stress-induced melting (Van Breemen et al., 2011). Several assumptions are introduced in the EGP formulation, starting with the multiplicative decomposition of the deformation gradient into elastic and plastic parts:

$$\boldsymbol{F} = \boldsymbol{F}_{\mathrm{e}} \cdot \boldsymbol{F}_{\mathrm{p}} \tag{9}$$

In this equation the *italic* font is used to distinguish the deformation gradient at the integration point level, from the homogenized deformation gradient of the RVE, Eq. (4). The plastic deformation is assumed volume preserving, i.e.:

$$J = \det(\boldsymbol{F}) = \det(\boldsymbol{F}_{\mathrm{e}}) \tag{10}$$

Yet another assumption says that the Cauchy stress is additively decomposed in three stress tensors:

$$\boldsymbol{\sigma} = \boldsymbol{\sigma}_{\mathrm{h}} + \boldsymbol{\sigma}_{\mathrm{r}} + \boldsymbol{\sigma}_{\mathrm{d}} \tag{11}$$

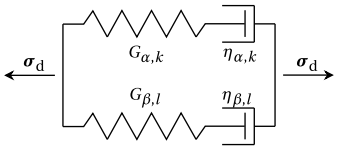

Fig. 3. Mechanical analog for driving stress of the EGP model; multiple Maxwell elements connected in parallel can also distinguish between two different relaxation processes: α and β.

where $\boldsymbol{\sigma}_\mathrm{h}$ is the hydrostatic, $\boldsymbol{\sigma}_\mathrm{r}$ the hardening, and $\boldsymbol{\sigma}_\mathrm{d}$ the driving stress tensor. The hydrostatic stress tensor is defined as:

$$\boldsymbol{\sigma}_\mathrm{h} = \kappa(J-1)\mathbf{I} \tag{12}$$

in which κ is the bulk modulus and $\mathbf{I}$ is the second-order unit tensor. The hardening stress tensor $\boldsymbol{\sigma}_\mathrm{r}$ represents the effect of reorientation of the molecular network in a loading process, and has the following form:

$$\boldsymbol{\sigma}_\mathrm{r} = \frac{1}{J} G_\mathrm{r} \tilde{\mathbf{B}}^\mathrm{d} \tag{13}$$

Here, G_r is the hardening modulus, whereas $\tilde{\mathbf{B}}^\mathrm{d}$ is the deviatoric part of the isochoric left Cauchy–Green deformation tensor defined as:

$$\tilde{\mathbf{B}} = J^{-2/3}\left(\boldsymbol{F}\cdot\boldsymbol{F}^\mathrm{T}\right) \tag{14}$$

One should note that there are alternative definitions of the hardening stress in the EGP, which may be elastic or viscoelastic (Senden et al., 2012).

Together with the hydrostatic stress, the driving stress represents intermolecular interactions of a polymer (Van Breemen et al., 2011). The mechanical analog for the driving stress of the EGP is shown in Fig. 3. This part of the total stress tensor admits multiple relaxation processes in the model, representing the thermorheologically complex behavior of the material (Klompen and Govaert, 1999). Each process may be modeled with multiple modes, that is with multiple Maxwell elements connected in parallel. Assuming two relaxation processes α and β, the definition of the driving stress tensor $\boldsymbol{\sigma}_\mathrm{d}$ reads (Khaleghi et al., 2022):

$$\begin{aligned}\boldsymbol{\sigma}_\mathrm{d} &= \sum_{k=1}^{p}\boldsymbol{\sigma}_{\alpha,k} + \sum_{l=1}^{q}\boldsymbol{\sigma}_{\beta,l}\\ &= \frac{1}{J}\sum_{k=1}^{p} G_{\alpha,k}\tilde{\mathbf{B}}^\mathrm{d}_{\mathrm{e}\alpha,k} + \frac{1}{J}\sum_{l=1}^{q} G_{\beta,l}\tilde{\mathbf{B}}^\mathrm{d}_{\mathrm{e}\beta,l}\end{aligned} \tag{15}$$

Here, $G_{x,j}$ is the shear modulus of Maxwell element j from process x, where x is either α or β and j is either k or l; $\tilde{\mathbf{B}}^\mathrm{d}_{\mathrm{e}x,j}$ is the deviatoric part of the isochoric elastic left Cauchy–Green deformation tensor in Maxwell element j belonging to process x; p and q represent the total number of α and β modes, respectively. To compute $\tilde{\mathbf{B}}^\mathrm{d}_{\mathrm{e}x,j}$ it is necessary to integrate the rate equation:

$$\dot{\tilde{\mathbf{B}}}_{\mathrm{e}x,j} = \left(\tilde{\mathbf{L}} - \mathbf{D}_{\mathrm{p}x,j}\right)\cdot\tilde{\mathbf{B}}_{\mathrm{e}x,j} + \tilde{\mathbf{B}}_{\mathrm{e}x,j}\cdot\left(\tilde{\mathbf{L}}^\mathrm{T} - \mathbf{D}_{\mathrm{p}x,j}\right) \tag{16}$$

where $\tilde{\mathbf{L}}$ is the isochoric velocity gradient and $\mathbf{D}_{\mathrm{p}x,j}$ is the plastic part of the rate of deformation tensor belonging to process x and Maxwell element j. This tensor is defined by introducing a constitutive relation of the following form:

$$\mathbf{D}_{\mathrm{p}x,j} = \frac{\boldsymbol{\sigma}_{x,j}}{2\eta_{x,j}(\bar{\tau}_x, p, S_x, T)} \tag{17}$$

where $\eta_{x,j}$ is the viscosity of the corresponding Maxwell element. In the context of the EGP model, the viscosity function motivated by the Eyring flow theory (Eyring, 1936) depends on the equivalent stress $\bar{\tau}_x$, the hydrostatic stress $p = -\kappa(J-1)$, the state parameter S_x and the absolute temperature T:

$$\eta_{x,j} = \eta_{0x,j}\frac{\bar{\tau}_x/\tau_{0x}}{\sinh(\bar{\tau}_x/\tau_{0x})}\exp\left(\frac{\mu_x p}{\tau_{0x}}\right)\exp(S_x)\exp\left[\frac{\Delta H_x}{R}\left(\frac{1}{T}-\frac{1}{T_\mathrm{ref}}\right)\right] \tag{18}$$

In this equation $\eta_{0x,j}$ is the initial viscosity of the corresponding Maxwell element, τ_{0x} the characteristic shear stress, μ_x the pressure dependency parameter, ΔH_x the activation enthalpy, R the gas constant, and $T_\mathrm{ref} = 298.15$ K is the reference absolute temperature. The equivalent stress reads:

$$\bar{\tau}_x = \sqrt{\frac{1}{2}\boldsymbol{\sigma}_x : \boldsymbol{\sigma}_x} \tag{19}$$

where $\boldsymbol{\sigma}_x = \sum\boldsymbol{\sigma}_{x,j}$. The characteristic shear stress reads:

$$\bar{\tau}_{0x} = \frac{k_\mathrm{B}T}{V_x} \tag{20}$$

in which k_B is the Boltzmann constant, and V_x is the activation volume.

The state parameter S_x takes into account the thermodynamic history of the material, and is defined as a product of the aging parameter S_ax and the softening function $R_{\gamma x}$ (Klompen et al., 2005). However, following earlier work on creep rupture (Kovačević et al., 2024), the aging parameter is set to zero.

Table 1
EGP model parameters.

κ [MPa]	G_r [MPa]	V_α [nm^3]	V_β [nm^3]	ΔH_α [kJ/mol]	ΔH_β [kJ/mol]	$\mu_\alpha = \mu_\beta$	$S_\alpha = S_\beta$
2600	25	3.518	3.518	375.87	325.28	0.08	0

Table 2
Relaxation spectrum of the EGP model.

x, j	$G_{x,j}$ [MPa]	$\eta_{0x,j}$ [MPa·s]
$\alpha, 1$	521.96	$1.992 \cdot 10^{26}$
$\beta, 1$	455.96	$4.965 \cdot 10^{22}$
$\beta, 2$	385.58	$5.518 \cdot 10^{21}$
$\beta, 3$	312.50	$6.761 \cdot 10^{20}$
$\beta, 4$	238.85	$2.108 \cdot 10^{19}$
$\beta, 5$	166.87	$1.591 \cdot 10^{15}$
$\beta, 6$	98.51	$2.571 \cdot 10^{12}$
$\beta, 7$	35.14	$7.086 \cdot 10^{9}$

In the EGP model, the equivalent plastic strain $\bar{\gamma}_p$ is obtained by integrating the corresponding rate equation:

$$\dot{\bar{\gamma}}_p = \frac{\bar{\tau}_{\alpha,1}}{\eta_{\alpha,1}} \equiv C, \quad \bar{\tau}_{\alpha,1} = \sqrt{\frac{1}{2}\boldsymbol{\sigma}_{\alpha,1} : \boldsymbol{\sigma}_{\alpha,1}} \tag{21}$$

where $\bar{\tau}_{\alpha,1}$ is the equivalent stress of the mode with the highest viscosity $\eta_{\alpha,1}$. For the sake of time homogenization procedure, this ratio is also denoted by C.

Since the time derivative of the isochoric elastic left Cauchy–Green deformation tensor, Eq. (16), is not an objective tensor, the formulation for the driving stress is cast into a form relying on the plastic right Cauchy–Green deformation tensor $\mathbf{C}_p$ that is invariant. A relation between this tensor and the tensor $\tilde{\mathbf{B}}_e$ can be derived. In the context of the Updated Lagrangian formulation, this relation in the modal form reads:

$$\mathbf{C}_{px,j} = \Delta\tilde{\boldsymbol{F}}^T \tilde{\mathbf{B}}_{ex,j}^{-1} \Delta\tilde{\boldsymbol{F}} \tag{22}$$

where $\Delta\tilde{\boldsymbol{F}}$ is the incremental isochoric deformation gradient. Once $\mathbf{C}_{px,j}$ at current time step is computed, Eq. (22) can be used to express $\tilde{\mathbf{B}}_{ex,j}$ that is further used in the driving stress update, Eq. (15). To this end, the rate equation for $\mathbf{C}_{px,j}$ is considered:

$$\dot{\mathbf{C}}_{px,j} = \frac{G_{x,j}}{\eta_{x,j}} \left(\Delta\tilde{\mathbf{C}} - \frac{1}{3}\mathrm{tr}\left(\bar{\tilde{\mathbf{B}}}_{ex,j}\right) \mathbf{C}_{px,j} \right) \tag{23}$$

Because the right Cauchy–Green deformation tensor and its derivatives are invariant, while the left Cauchy–Green deformation tensor is objective, the rotation neutralized version of $\tilde{\mathbf{B}}_{ex,j}$ is considered in the previous equation, which is defined as:

$$\bar{\tilde{\mathbf{B}}}_{ex,j} = \Delta\mathbf{R}^T \tilde{\mathbf{B}}_{ex,j} \Delta\mathbf{R} \tag{24}$$

Assuming that $\mathrm{tr}(\bar{\tilde{\mathbf{B}}}_{ex,j})/3 \approx 1$ in Eq. (23), the expression for $\mathbf{C}_{px,j}$ at current time step n can be derived as:

$$\mathbf{C}_{px,j}^n = (1 - \lambda_{x,j}^n)\Delta\tilde{\mathbf{C}}^n + \lambda_{x,j}^n \mathbf{C}_{px,j}^{n-1} \tag{25}$$

where the plasticity parameter $\lambda_{x,j}^n$ measures the amount of plastic deformation in the time step and emerges as:

$$\lambda_{x,j}^n = \frac{1}{1 + \Gamma_{x,j}^n \Delta t} \tag{26}$$

where $\Gamma_{x,j}^n = G_{x,j}/\eta_{x,j}^n$ is the ratio between the modal shear modulus and viscosity, and Δt is the time increment. When $\lambda_{x,j}^n = 1$ the deformation increment is purely elastic; when $\lambda_{x,j}^n = 0$ the increment is completely plastic. The modal plasticity parameters depend on the viscosity through $\Gamma_{x,j}^n$, which in turn depends on the equivalent stress that defines the equivalent plastic strain rate, Eq. (21). With this in mind, a coupled system of equations is iteratively solved, whereby the plasticity parameters are computed together with the equivalent plastic strain, assuming the backward Euler integration scheme:

$$\begin{aligned} &\lambda_{x,j}^n \left(1 + \Gamma_{x,j}^n \Delta t\right) = 1 \\ &\bar{\gamma}_p^n - \dot{\bar{\gamma}}_p^n \Delta t = \bar{\gamma}_p^{n-1} \end{aligned} \tag{27}$$

Values of the model parameters used in this work are listed in Table 1, followed by the relaxation spectrum in Table 2. All these EGP model inputs are the same as in Kovačević et al. (2024).

3.2. Two-scale Eindhoven Glassy polymer constitutive model

In this work, a two-scale version of the EGP model is developed to efficiently take into account the high-cycle loading scenario. Following the concept of time homogenization (TH), see e.g. Rocha et al. (2019), Yu and Fish (2002), Oskay and Fish (2004) and Haouala and Doghri (2015), the model distinguishes between two timescales: micro timescale (t_μ) and macro timescale (t_M). In that

regard, the physical time t is represented as a combination of the slowly varying time coordinate t_M and the rapidly varying time coordinate t_μ:

$$t = t_M + T t_\mu \tag{28}$$

where T is the load period and $t_\mu \in [0, 1]$. With this decomposition in mind, any field variable ζ can be expressed as a function of the initial position $\mathbf{X}$ and two time coordinates: $\zeta(\mathbf{X}, t_M, t_\mu)$. Since the whole consideration concerns an integration point initially located at $\mathbf{X}$, the position coordinate is dropped from further equations. The total derivative of ζ with respect to the physical time then reads:

$$\dot{\zeta} = \frac{\partial \zeta}{\partial t_M} + \frac{1}{T}\frac{\partial \zeta}{\partial t_\mu} \tag{29}$$

The field variable ζ can be asymptotically expanded in a series:

$$\zeta(t_M, t_\mu) = \sum_{i=0}^{\infty} T^i \zeta_i(t_M, t_\mu) \tag{30}$$

where $\zeta_i(t_M, t_\mu)$ is almost periodic in t_μ due to the evolving viscosity in the EGP model, and its relative contribution to ζ decays as the power i increases.

If a field quantity, e.g. the equivalent plastic strain rate in Eq. (21), admits a gradient at a point, its first-order asymptotic expansion can be written as the following (Haouala and Doghri, 2015):

$$C = C_0 + T\, DC(\bar{\tau}_0, \eta_0) \cdot (\bar{\tau}_1, \eta_1) + O(T^2) \tag{31}$$

where O is the Landau notation for higher-order terms, $DC(\bar{\tau}_0, \eta_0) \cdot (\bar{\tau}_1, \eta_1)$ is the inner product of the gradient of C with respect to $\bar{\tau}_0$ and η_0 with the corresponding quantities of the order 1 ($\bar{\tau}_1$, η_1). The subscripts here should not be confused with different modes of the EGP model: they represent quantities of different order associated with the mode of highest viscosity. Applying the asymptotic expansion on $\bar{\gamma}_\mathrm{p}$ and performing the total time differentiation, Eqs. (30) and (29), yields an expression for the equivalent plastic strain rate:

$$\dot{\bar{\gamma}}_\mathrm{p} = \frac{\partial \bar{\gamma}_\mathrm{p0}}{\partial t_M} + \frac{1}{T}\frac{\partial \bar{\gamma}_\mathrm{p0}}{\partial t_\mu} + T\frac{\partial \bar{\gamma}_\mathrm{p1}}{\partial t_M} + \frac{\partial \bar{\gamma}_\mathrm{p1}}{\partial t_\mu} + T\frac{\partial \bar{\gamma}_\mathrm{p2}}{\partial t_\mu} + O(T^2) \tag{32}$$

If we now group the terms of the same order of T in Eqs. (31) and (32) the following relations are obtained (up to order 0):

$$\begin{aligned} &\left(T^{-1}\right) : \frac{\partial \bar{\gamma}_\mathrm{p0}}{\partial t_\mu} = 0 \\ &\left(T^{0}\right) : \frac{\partial \bar{\gamma}_\mathrm{p0}}{\partial t_M} + \frac{\partial \bar{\gamma}_\mathrm{p1}}{\partial t_\mu} = C_0 \end{aligned} \tag{33}$$

It follows from the (T^{-1}) problem that the zero-order equivalent plastic strain does not evolve with the micro time coordinate, i.e., $\bar{\gamma}_\mathrm{p0} = \bar{\gamma}_\mathrm{p0}(t_M)$. Further, $\partial \bar{\gamma}_\mathrm{p1}/\partial t_\mu \approx 0$ in Eq. (33), since $\bar{\gamma}_\mathrm{p1}$ is almost periodic in t_μ and the equivalent plastic strain is a non-decreasing function. Therefore, by solving the zero-order problem we update the material state elastically at t_μ, and account for viscoplastic deformation at t_M, i.e., at macro time steps. Because the analysis is geometrically nonlinear, it is still necessary to utilize an iterative Newton–Raphson solver at micro time steps.

3.2.1. *Effective time increment*

At the micro timescale, the cyclic variation of the load is accounted for, but the constitutive response is simplified. At the macro timescale, a constant load is applied and the complete constitutive model is used, but information from the micro time steps is used to perform the update. The stress-dependent plastic flow is averaged over the load cycle by replacing Δt in Eq. (27) with an effective time increment Δt_eff.

One load cycle with the proposed time stepping scheme is illustrated in Fig. 4, where the load period coincides with the time increment Δt. The loading cycle is divided into micro time steps at which the information necessary to compute Δt_eff for the macro time step is collected. The material update at micro time steps is elastic, without evolution in viscoplastic deformation, which means that $\lambda^n_{x,j} = 1$, see Eq. (25). However, in order to compute the effective time increment at an integration point, $\dot{\bar{\gamma}}_\mathrm{p}$ is computed from Eq. (21) in the elastic micro time steps. Also, symmetry is used at t_μ, such that $\dot{\bar{\gamma}}_\mathrm{p}$ is mirrored to the corresponding micro time step, see Fig. 4.

When all micro time steps for a single cycle are completed, a macro time step is made, with a jump from the previous converged macro time step to the current one. Macro time steps $n-1$ and n correspond to the same load level, that is $\sigma^{\max}_{yy}$ in this case. If no information is conveyed from micro time steps, the standard update of the EGP model would lead to a creep response, with the actual time increment Δt. In order to include the effect of cyclic loading, an effective time increment is introduced to correct for the variation in equivalent plastic strain rate over the cycle:

$$\dot{\bar{\gamma}}^n_\mathrm{p} \Delta t_\mathrm{eff} = \int_{t^{n-1}}^{t^n} \dot{\bar{\gamma}}_\mathrm{p}\, dt \tag{34}$$

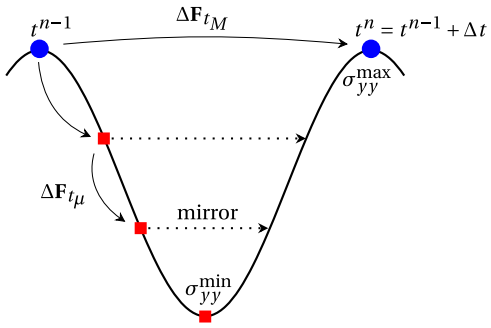

Fig. 4. One load cycle divided in micro time steps (squares) and macro time steps (circles); increment in deformation gradient $\Delta \mathbf{F}_{t_\mu}$ computed with respect to previous converged macro time step for the first micro time step, and with respect to previous micro time step for other micro time steps; $\Delta \mathbf{F}_{t_M}$ computed with respect to previous converged macro time step.

Table 3
Elastic constants of the transversely isotropic constitutive model.

E_1 [GPa]	E_2 [GPa]	G_{12} [GPa]	ν_{12}	ν_{23}
125	15	5	0.05	0.3

where the integral on the right hand side is evaluated with a trapezoidal integration rule using $\dot{\bar{\gamma}}_\mathrm{p}$ from the micro time steps of the last cycle, as well as from the previous and current macro time steps, $\dot{\bar{\gamma}}_\mathrm{p}^{n-1}$ and $\dot{\bar{\gamma}}_\mathrm{p}^{n}$, respectively. From Eq. (34) the expression for Δt_eff emerges as:

$$\Delta t_\mathrm{eff} = \frac{\int_{t^{n-1}}^{t^n} \dot{\bar{\gamma}}_\mathrm{p} dt}{\dot{\bar{\gamma}}_\mathrm{p}^{n}} \tag{35}$$

The concept of effective time in the EGP model was used by Janssen et al. (2008a) to capture the endurance limit in polymers at cyclic loading. It was computed employing stress- and temperature-based shift functions on the actual time, and used to evolve the aging parameter in a phenomenological way. Despite the similar terminology in Janssen et al. (2008a), our approach shows more resemblance to another paper by Janssen et al. (2008b), in which the so-called acceleration factor was computed as the ratio of the incremental equivalent plastic strain in cyclic loading to that in static loading, for one typical load cycle. The acceleration factor eventually multiplies the plastic strain rate due to static stress, in an analytical framework (not used in the EGP model) determining the time to failure in static as well as in cyclic loading. In our case, the product of the effective time increment and the equivalent plastic strain rate in static loading equals an increment in the equivalent plastic strain due to cyclic loading, Eq. (34).

3.3. Transversely isotropic constitutive model for carbon fibers

Assuming absence of failure in the reinforcement, we use a hyperelastic transversely isotropic constitutive model for carbon fibers formulated by Bonet and Burton (1998), with a minor modification reported in Kovačević and Van der Meer (2022). Since no additional changes are made to the model, only the elastic constants used to run simulations are listed here, see Table 3. The adopted values are the same as in Kovačević et al. (2024). E_1 is the Young's modulus in the preferential stiffness direction of the material, that is the fiber direction in this case; E_2 and ν_{23} are the Young's modulus and the Poisson's ratio defining the material behavior in the plane of isotropy; G_{12} and ν_{12} are the shear modulus and the Poisson's ratio for the planes perpendicular to the isotropic plane.

3.4. Fatigue cohesive zone model

To model microcrack propagation through the polymer matrix under the high- and low-cycle fatigue loading we utilize the cohesive zone model formulated by Dávila (2020), in its implicit formulation with consistent linearization by Hofman et al. (2024). Dávila's model, originally developed for problems of delamination in composites, assumes a damage variable which grows with either quasi-static or fatigue loading. It is meant to represent creation of microcracks at a lower scale of observation. We apply the same CZM in the RVE, also assuming that the damage variable represents corresponding cracking processes in the polymer matrix at a yet lower scale.

The cohesive model is formulated in local orthonormal coordinate frame $(\mathbf{n}, \mathbf{s}, \mathbf{t})$, which defines the orientation of the cohesive surface at the integration point: $\mathbf{n}$ is the unit vector in the normal direction associated with the normal dummy stiffness K_n; $\mathbf{s}$ and $\mathbf{t}$ are the unit vectors tangent to the surface, associated with the shear dummy stiffness K_{sh}. Cohesive segments are inserted on the fly (Camacho and Ortiz, 1996) when a suitable initiation criterion is satisfied, meaning that zero displacement jump corresponds

with a nonzero traction vector. Because this combination may lead to the singularity problem in mixed-mode loading (Van der Meer and Sluys, 2009), the cohesive model is evaluated with the shifted displacement jump $[\![\mathbf{u}]\!]$ (Hille et al., 2009):

$$[\![\mathbf{u}]\!] = [\![\mathbf{u}]\!]^{\text{fe}} + [\![\mathbf{u}]\!]^{0} \tag{36}$$

where $[\![\mathbf{u}]\!]^{\text{fe}}$ is the displacement jump obtained from the finite element space, and $[\![\mathbf{u}]\!]^{0}$ is the displacement shift:

$$[\![\mathbf{u}]\!]^{0} = \left(\frac{t_n^0}{K_n}, \frac{t_s^0}{K_{\text{sh}}}, \frac{t_t^0}{K_{\text{sh}}} \right)^{\text{T}} \tag{37}$$

with t_n^0, t_s^0, t_t^0 the traction vector components at initiation.

3.4.1. Quasi-static damage

The evolution of damage under quasi-static loading is described with Turon's cohesive model (Turon et al., 2018), which can be written in the following form:

$$\mathbf{t} = (\mathbf{I} - \boldsymbol{\Omega})\mathbf{K}[\![\mathbf{u}]\!] = (\mathbf{I} - \boldsymbol{\Omega})\mathbf{t}^{\text{eff}} \tag{38}$$

where $\mathbf{t}^{\text{eff}}$ is the effective traction on the cohesive surface; $\mathbf{I}$ is the identity matrix and $\mathbf{K}$ is the dummy stiffness matrix:

$$\mathbf{K} = \begin{bmatrix} K_n & 0 & 0 \\ 0 & K_{sh} & 0 \\ 0 & 0 & K_{sh} \end{bmatrix} \tag{39}$$

In Eq. (38), $\boldsymbol{\Omega}$ is the damage tensor defined as:

$$\Omega_{ij} = d\delta_{ij} \left(1 + \delta_{i1} \frac{\langle -t_n^{\text{eff}} \rangle}{t_n^{\text{eff}}} \right) \tag{40}$$

The Kronecker delta δ_{ij} ensures nonzero components only on the main diagonal of $\boldsymbol{\Omega}$, while the Macaulay brackets restore the dummy stiffness in the normal direction, in the case of compression. The damage variable d measures the stiffness loss in a mixed-mode loading scenario, and its thermodynamically consistent evolution is ensured by relating the dummy stiffnesses:

$$K_{sh} = K_n \frac{G_{Ic}}{G_{IIc}} \left(\frac{f_{sh}}{f_n} \right)^2 \tag{41}$$

Here, G_{Ic} and G_{IIc} are the fracture energies for the mode I and mode II loading, while f_n and f_{sh} are the quasi-static strength parameters in the normal and shear direction, respectively. To compute the stiffness loss d, the cohesive model can be represented with an equivalent 1D traction-separation relation:

$$\sigma = (1 - d) K_{\mathcal{B}} \Delta \tag{42}$$

where σ is the equivalent stress, $K_{\mathcal{B}}$ the mixed-mode dummy stiffness, and Δ is the equivalent displacement jump. The mixed-mode dummy stiffness reads:

$$K_{\mathcal{B}} = (1 - \mathcal{B}) K_n + \mathcal{B} K_{sh} \tag{43}$$

where $\mathcal{B}$ is the mode-mixity variable defined as:

$$\mathcal{B} = \frac{K_{sh}[\![u]\!]_{sh}^2}{K_n \langle [\![u]\!]_n \rangle^2 + K_{sh}[\![u]\!]_{sh}^2} \tag{44}$$

In this expression $[\![u]\!]_{sh}$ is the Euclidean norm of the displacement jump sub-vector corresponding with the shear components:

$$[\![u]\!]_{sh}^2 = [\![u]\!]_s^2 + [\![u]\!]_t^2 \tag{45}$$

The equivalent stress σ is defined as:

$$\sigma = \left[\langle t_n \rangle^2 + t_s^2 + t_t^2 \right]^{1/2} \tag{46}$$

whereas the equivalent displacement jump emerges as:

$$\Delta = \frac{K_n \langle [\![u]\!]_n \rangle^2 + K_{sh}[\![u]\!]_{sh}^2}{\left[K_n^2 \langle [\![u]\!]_n \rangle^2 + K_{sh}^2 [\![u]\!]_{sh}^2 \right]^{1/2}} \tag{47}$$

To track the damage process, the state variable $\mathcal{D}$ is introduced as an energy-based damage variable:

$$\mathcal{D} \equiv \frac{G_d}{G_c} = \frac{\Delta - \Delta_0}{\Delta_f - \Delta_0} \tag{48}$$

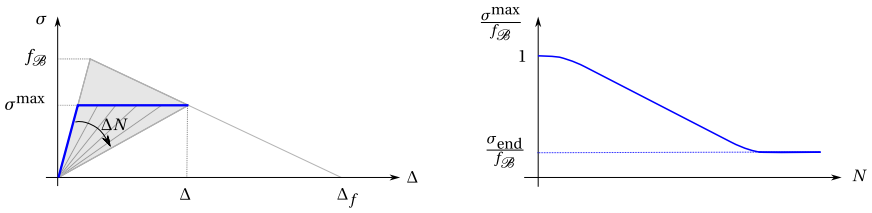

Fig. 5. The quasi-static cohesive model (Turon et al., 2018) represents the failure envelope of the traction-separation response in fatigue loading (left). The evolution of fatigue damage is such that the CZM is able to reproduce an S-N curve, but does not account for actual loading frequency (right).

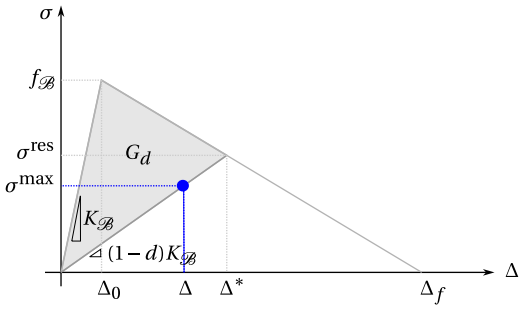

Fig. 6. Graphical representation of the quantities used in formulation of fatigue cohesive zone model.

$\mathcal{D}$ represents the ratio between the dissipated energy G_d and the fracture energy G_c, and alternatively can be written as a function of the equivalent displacement jump. The state variable is evaluated by knowing the equivalent displacement jump at initiation Δ_0, and at the moment of fracture Δ_f:

$$\begin{aligned}\Delta_0 &= \left[\frac{K_n(\llbracket u\rrbracket_n^0)^2 + \left(K_{sh}(\llbracket u\rrbracket_{sh}^0)^2 - K_n(\llbracket u\rrbracket_n^0)^2\right)\mathcal{B}^{\eta_{\text{BK}}}}{K_{\mathcal{B}}}\right]^{1/2}\\ \Delta_f &= \frac{K_n\llbracket u\rrbracket_n^0\llbracket u\rrbracket_n^f + \left(K_{sh}\llbracket u\rrbracket_{sh}^0\llbracket u\rrbracket_{sh}^f - K_n\llbracket u\rrbracket_n^0\llbracket u\rrbracket_n^f\right)\mathcal{B}^{\eta_{\text{BK}}}}{K_{\mathcal{B}}\Delta_0}\end{aligned} \tag{49}$$

In this equation η_{BK} is the Benzeggagh–Kenane (B-K) interaction parameter (Benzeggagh and Kenane, 1996), while the pure mode I and the pure mode II displacement jump at initiation (superscript 0) and the moment of fracture (superscript f) are defined as:

$$\begin{aligned}\llbracket u\rrbracket_n^0 &= \frac{f_n}{K_n}, \qquad \llbracket u\rrbracket_n^f = \frac{2G_{Ic}}{f_n}\\ \llbracket u\rrbracket_{sh}^0 &= \frac{f_{sh}}{K_{sh}}, \qquad \llbracket u\rrbracket_{sh}^f = \frac{2G_{IIc}}{f_{sh}}\end{aligned} \tag{50}$$

Finally, the relation between the energy-based damage variable $\mathcal{D}$ and the damage variable d is:

$$d = 1 - \frac{(1-\mathcal{D})\Delta_0}{\mathcal{D}\Delta_f + (1-\mathcal{D})\Delta_0} \tag{51}$$

3.4.2. Fatigue damage

Taking the quasi-static cohesive model as the failure envelope, Dávila formulated a fatigue cohesive zone model (Dávila, 2020). In the model, the state variable $\mathcal{D}$ may evolve before the quasi-static strength $f_{\mathcal{B}}$ is reached, given an increment in the number of load cycles ΔN. When the pair $(\sigma^{\max}, \Delta)$ reaches the softening line of the quasi-static CZM, failure of the material ensues, see Fig. 5 (left). The fatigue damage variable $\mathcal{D}_f$ is defined in such a way that the model reproduces the S-N curve of the material, but without considering effects of the actual loading frequency. The fatigue damage changes with the number of cycles N according to the evolution law:

$$\frac{\mathrm{d}\mathcal{D}_f}{\mathrm{d}N} = f_{\mathcal{D}}(\Delta, \Delta^*, \mathcal{D}) \tag{52}$$

where Δ^* is the equivalent displacement jump corresponding with the residual strength σ^{res}, see Fig. 6, defined as:

$$\Delta^* = \mathcal{D}(\Delta_f - \Delta_0) + \Delta_0 \tag{53}$$

Table 4
Values of cohesive zone model parameters; last three related to fatigue damage.

K_n [N/mm^3]	G_{Ic} [N/mm]	G_{IIc} [N/mm]	f_n [N/mm^2]	f_{sh} [N/mm^2]	η_{BK}	ϵ	η	p
10^8	0.03	0.095	117.5	80	2.284	0.5	0.39	$\beta+1$

To make sure that the traction-separation curve in fatigue scenarios remains inside the failure envelope, the quasi-static damage variable $\mathcal{D}_s$ is also computed:

$$\mathcal{D}_s = \frac{\Delta - \Delta_0}{\Delta_f - \Delta_0} \tag{54}$$

Finally, the state variable $\mathcal{D}$ is the maximum of $\mathcal{D}_s$ and $\mathcal{D}_f$:

$$\mathcal{D} = \max\left(\mathcal{D}_s, \mathcal{D}_f\right) \tag{55}$$

The fatigue damage function, Eq. (52), is integrated numerically using the trapezoidal rule (Hofman et al., 2024):

$$\mathcal{D}_f^n = \mathcal{D}_f^{n-1} + \frac{1}{2}\Delta N\left[f_{\mathcal{D}}^{n-1} + f_{\mathcal{D}}^n\right] \tag{56}$$

The evolution of fatigue damage, Eq. (52), is represented with the CF20 function (Joosten et al., 2022):

$$f_D^{\mathrm{CF20}} = \frac{1}{\gamma}\frac{(1-\mathcal{D})^{\beta-p}}{E^\beta(p+1)}\left(\frac{\Delta}{\Delta^*}\right)^\beta \tag{57}$$

Here, $\gamma = 10^7$ is the number of cycles without failure at the relative endurance limit E, p is a fitting parameter adopted as: $p = \beta + 1$, and β is the parameter defining the slope of the S-N curve:

$$\beta = \frac{-7\eta}{\log E} \tag{58}$$

In this equation, η is the brittleness parameter which marks the kink in the S-N curve, that distinguishes between the low-cycle fatigue and the high-cycle fatigue regime. The relative endurance limit is defined as:

$$E = \frac{2C_l\epsilon}{C_l\epsilon + 1 + R(C_l\epsilon - 1)} \tag{59}$$

where ϵ is the relative endurance limit at $R = -1$ and mode I loading, while C_l is the correction factor that takes into account mixed-mode loading (Juvinall and Marshek, 2020):

$$C_l = 1 - 0.42\mathcal{B} \tag{60}$$

To evaluate Eq. (59) the load ratio R is computed locally for every cohesive surface, following the idea presented by Joosten et al. (2022). With a small adjustment that the Macaulay operation is not performed on t_n, the severity vector is defined as:

$$\bar{S} = \left(\frac{t_n}{f_n}, \frac{t_s}{f_{\mathrm{sh}}}, \frac{t_t}{f_{\mathrm{sh}}}\right)^{\mathrm{T}} \tag{61}$$

In a loading scenario where the only nonzero traction component is t_n and the Macaulay brackets are included, it is not possible to distinguish between $R = 0$ and negative R. Eventually, R is computed as:

$$R = \frac{\bar{S}^{\min} \cdot \bar{S}^{\max}}{\|\bar{S}^{\max}\|^2} \tag{62}$$

where $\bar{S}^{\min}$ and $\bar{S}^{\max}$ are the minimum and the maximum severity vector encountered in one loading cycle, respectively. For this purpose, the severity vectors computed at t^{n-1} macro time step and at the micro time step with the minimum applied stress are utilized ($\bar{S}_M$ and $\bar{S}_\mu$, respectively). Of these two vectors, the one with larger Euclidean norm is assigned to $\bar{S}^{\max}$ in Eq. (62).

Parameters used to run simulations with the presented cohesive model are tabulated in Table 4, where the last three parameters are related to the fatigue damage part. The dummy stiffness acquires the high value in order to reduce the compliance effect introduced in the RVE by the presence of many cohesive segments. The fracture energies are adopted according to Kovačević et al. (2022). The relation for p follows the form presented in Raimondo et al. (2022). The B-K interaction parameter has a value according to Turon et al. (2006). The strength parameters f_n and f_{sh}, as well as the fatigue damage parameters ϵ and η, are calibrated on experimental S-t curves for $R = 0.1$, $f = 1$ Hz, $\chi = 90°$ and $\chi = 45°$, see Section 5.2.

3.5. Cohesive microcrack initiation

Inter-element cohesive segments are included in the RVE on the fly, when an initiation criterion is satisfied. Dealing with the low- and high-cycle fatigue, in this study we use the endurance limit-based initiation criterion introduced in Hofman et al. (2024). In the criterion, the equivalent endurance limit (stress) is defined as:

$$\sigma_{\mathrm{end}} = E f_{\mathcal{B}} \tag{63}$$

where E is computed with Eq. (59), and $f_{\mathcal{B}}$ is the mode-dependent quasi-static strength, $f_{\mathcal{B}} = K_{\mathcal{B}}\Delta_0$. It can be expressed in terms of the cohesive model input parameters and the mixed-mode variable $\mathcal{B}$:

$$f_{\mathcal{B}} = \left(\left[(1-\mathcal{B})K_n + \mathcal{B}K_{sh}\right]\left[f_n^2/K_n + \left(f_{sh}^2/K_{sh} - f_n^2/K_n\right)\mathcal{B}^{\eta_{\mathrm{BK}}}\right]\right)^{1/2} \tag{64}$$

When the cohesive initiation criterion is checked, the corresponding cohesive segment is not present and the displacement jump is a zero vector. Therefore, the direct application of Eq. (44) to compute $\mathcal{B}$ is not possible, and $\mathcal{B}$ is expressed through the traction vector components on a potential cohesive surface:

$$\mathcal{B} = \frac{t_{sh}^2/K_{sh}}{\langle t_n\rangle^2/K_n + t_{sh}^2/K_{sh}} \tag{65}$$

where a potential cohesive surface is any surface between bulk finite elements in the matrix, or on the fiber/matrix interface, and the traction vector is obtained from the local stress as $\mathbf{t} = \boldsymbol{\sigma}\mathbf{n}$. Finally, a cohesive segment will initiate if the equivalent stress on the potential cohesive surface, Eq. (42), is larger than the relative endurance limit stress:

$$\frac{\sigma}{\sigma_{\mathrm{end}}} > 1 \tag{66}$$

In this study we introduce a modification when checking for cohesive initiation by not letting the R used for computing E exceed a value of 0.1, i.e., for the initiation criterion $E(R)$ is replaced with $E(\min(R, 0.1))$. The reason for this constraint can be explained considering the creep rupture problem. In that case $R = 1 \rightarrow E = 1$, and $\sigma_{\mathrm{end}} = f_{\mathcal{B}}$ in Eq. (63). By setting the initiation threshold to quasi-static strength a large range of applied stresses is cut off from possible creep rupture. Therefore, we found this adaptation to be crucial for obtaining creep rupture at relevant stress levels. In this regard, the value of 0.1 was prescribed, but detailed sensitivity analysis on its value was not performed.

Given the endurance limit based initiation criterion, cohesive segments may initiate almost everywhere in the matrix and the fiber/matrix interface, see Section 5.2.3. To reduce computational complexity, cohesive initiation is allowed if the angle between a potential cohesive surface normal and the projection of maximum principal stress in the $\boldsymbol{e}_2$-$\boldsymbol{e}_3$ plane (plane perpendicular to the fiber direction, see Fig. 2) is less than 45°.

4. Adaptive time stepping

The time stepping procedure outlined in the two-scale EGP formulation (Fig. 4) is part of a bigger, adaptive time stepping scheme. In this scheme, time increments between macro time steps vary depending on the convergence rate of the global Newton–Raphson scheme. If the number of iterations in a converged macro time step is less than a prescribed optimal number of iterations, the time increment of the next macro time step will increase, and vice versa. The change in time increment is according to (Verhoosel et al., 2009):

$$\Delta t^n = \Delta t^{n-1}\left(\frac{1}{2}\right)^{\left(n_{\mathrm{iter}}^{n-1} - n_{\mathrm{iter}}^{\mathrm{opt}}\right)/4} \tag{67}$$

where n_{iter}^{n-1} is the number of iterations in the last converged macro time step, and $n_{\mathrm{iter}}^{\mathrm{opt}}$ is the prescribed optimal number of iterations. The updated time increment is then used to evaluate the integral in Eq. (35), to obtain the effective time increment for the bulk material.

This computational procedure assumes that the time increment equals the loading period T, which is then changing throughout the analysis. This change in T is obviously in contrast with the experimental situation, where T (or the load frequency f) is constant. The assumption of changing T in the simulation can be introduced given the fact that the EGP response under cyclic loading is largely frequency independent. To support this statement, the full-field response of a single hexahedral finite element with the EGP model subject to different loading frequencies, with load ratio $R = 0.1$ and engineering stress $\sigma^{\max} = 90$ MPa, is shown in Fig. 7. As observed from the figure, there is practically no influence of f on the time-dependent response. A very minor influence is observed for the evolution of the strain at $\sigma^{\min}$, and even less for the evolution of the strain at $\sigma^{\max}$. This frequency independence allows for adaptive time stepping and taking that $\Delta t = T$, because the time homogenized response aims at capturing the maximum deformation in the matrix. Note that changing the load frequency also changes the strain rate, and the results in Fig. 7 show that the total accumulation of viscous deformation over time under cyclic loading does not have a strong dependence on loading rate.

Given the elastic updates at micro time steps (t_μ), the time increment size is irrelevant for these computations, and the data collected at t_μ for computing the effective time increment is not altered if the macro time update is repeated due to the lack of convergence. Other implications of elastic updates at t_μ are that cohesive initiation is not allowed, and that the cycle increment to the cohesive model is nonzero only at t_M. Given the actual time increment, the cycle increment at macro time steps is computed as:

$$\Delta N^n = \Delta t^n \cdot f \tag{68}$$

where f has a constant value equal to the actual frequency in the analysis. With $\Delta N \neq 0$ only at macro time steps, the fatigue cohesive model can also be regarded as *time-homogenized*. Although not derived from the TH formalism, see Section 3.4, by following the similar reasoning as in Section 3.2, it can be shown that in the zero-order approximation (T^0) the fatigue damage variable does not evolve with t_μ, i.e., $\mathcal{D}_f = \mathcal{D}_f(t_M)$.

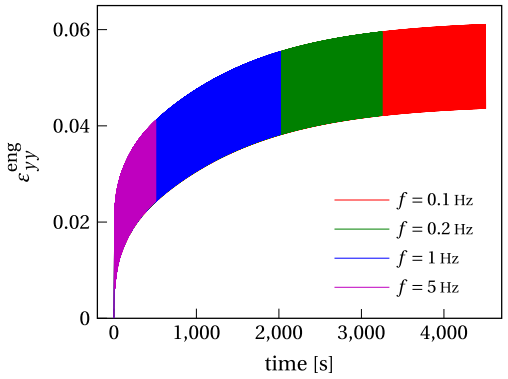

Fig. 7. Strain response of single finite element with EGP model under uniaxial cyclic loading, where engineering stress $\sigma^{\max} = 90$ MPa and $R = 0.1$.

Table 5
Algorithm for adaptive time step n.

(1) update Δt, Eq. (67)
(2) perform $n_\mu/2$ micro time steps
  - record $\dot{\bar{\gamma}}_{\text{p}}$, Eq. (21); elastic update of the matrix; no damage evolution in CZM
(3) macro time update; matrix plasticity with Δt_{eff} from Eq. (35); cohesive initiation with Eq. (66) and damage evolution with ΔN from Eq. (68)
  - if converged, go to (1)
  - if not converged, reduce Δt and repeat (3)

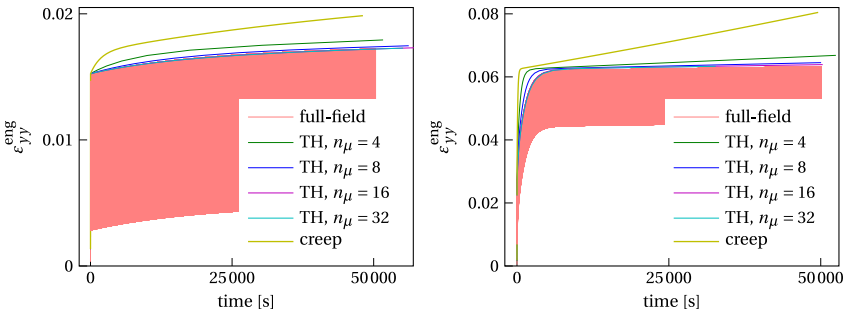

Fig. 8. EGP response under uniaxial cyclic loading: $R = 0.1$, $\sigma^{\max} = 70$ MPa (left) and $\sigma^{\max} = 90$ MPa (right); full-field response compared with TH response for different number of micro time steps; the creep response corresponding to $\sigma^{\max}$ is also included.

An algorithm for update of material models in one time step is shown in Table 5. Other implementation details on setting the external force vector, checking for cohesive initiation, etc., can be found in Kovačević et al. (2024), that is based on the algorithm presented in Van der Meer (2012). The model is implemented in Jive: a C++ library aimed for numerical simulations (Nguyen-Thanh et al., 2020).

5. Results and discussion

5.1. Time homogenization

The performance of the model is checked with several examples. In all reported cases cyclic engineering stress is applied. To begin with, the accuracy of the time homogenization procedure is examined on a single hexahedral finite element with the EGP material model. The time homogenized response for different number of micro time steps n_μ is compared with the fully-resolved response, which is evaluated with the constant time step of $T/40$ at a frequency of 0.1 Hz. The results are plotted in Fig. 8, for $R = 0.1$ and two maximum stress levels, where the creep response for the same stress level (at $R = 1$) is also included. As noticed from the figure, all time homogenized cases yield a lower strain compared to the creep response, which is in line with the observation that less plastic strain accumulates in cyclic loading. Furthermore, as the number of micro time steps increases, the TH response approaches the full-field response. For $\sigma^{\max} = 70$ MPa already at $n_\mu = 16$ the TH response matches the reference result. For $\sigma^{\max} = 90$ MPa, however, much more plastic deformation develops during cyclic loading and the TH response slightly deviates from the reference result: for $n_\mu = 16$ the relative error in the $\varepsilon^{\text{eng}}_{yy}$ at $t = 5 \cdot 10^4$ s is 0.74%.

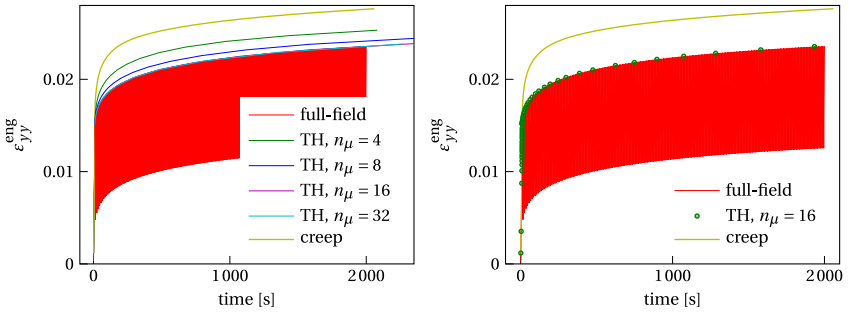

Fig. 9. Unit cell RVE under cyclic loading: $R = 0.1$, $\sigma^{\max}_{yy} = 100$ MPa, $\chi = 45°$; creep and full-field cyclic response ($f = 0.1$ Hz) compared with TH response for different number of micro time steps (left); TH response in scatter form illustrates adaptive stepping (right).

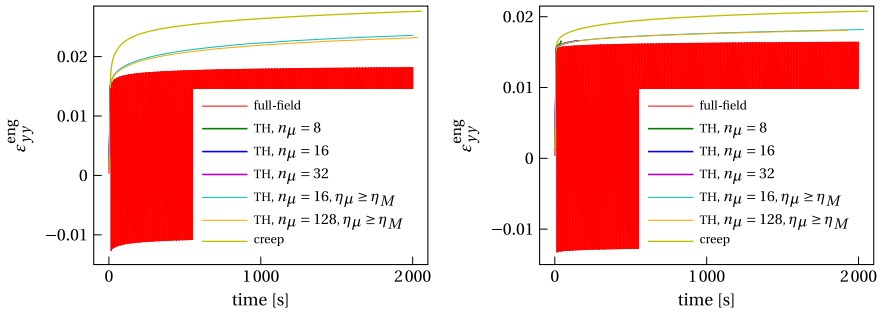

Fig. 10. Unit cell RVE under cyclic loading: $R = -1$, $\sigma^{\max}_{yy} = 100$ MPa, $\chi = 45°$ (left), $\chi = 90°$ (right); TH response compared with creep and full-field cyclic results; η_μ is viscosity computed at micro time steps and η_M is viscosity from last macro time step.

The accuracy of the TH procedure is also checked on a unit cell RVE. Finite elements representing bulk material are 12-node wedge-shaped elements, while, if present, cohesive zones are represented with 12-node cohesive elements (Kovačević et al., 2022). The unit cell consisting of 274 finite elements with the minimum element length of 0.7 μm is loaded under 45°. The maximum engineering stress in the global loading direction is $\sigma^{\max}_{yy} = 100$ MPa, see Fig. 1, the load ratio is $R = 0.1$ and cohesive segments are not included. Comparison of the TH results with the full-field cyclic and creep response is shown in Fig. 9 (left). It is concluded again that increasing n_μ leads to more accurate TH results, with convergence around $n_\mu = 16$. In Fig. 9 (right), the TH response for $n_\mu = 16$ is plotted with markers to indicate the adaptive time stepping feature of the model. If significant plastic deformation develops in the model, the time step size is reduced to properly capture the equilibrium path, whereas in the absence of significant plastic deformation, or nonlinearity in general, the time step size is enlarged.

However, the TH procedure is not accurate in all loading situations. Let us consider the case where $R = -1$ and $\sigma^{\max}_{yy} = 100$ MPa, meaning that significant plastic deformation develops also at reversed loading. The creep and full-field cyclic response are compared with TH results for two loading angles, $\chi = 45°$ and $\chi = 90°$, see Fig. 10. It follows from the figure that the TH procedure is unstable: in the 45° case it fails to enter the cyclic loading phase, while in the 90° case the TH procedure fails quickly after the cyclic loading is started. The reason for this instability lies in the elastic updates at micro time steps, where the neglect of significant plastic deformation in the material leads to an overestimated equivalent stress and, correspondingly, to a lower viscosity, Eq. (18). Consequently, the equivalent plastic strain rate, Eq. (21), computed at micro time steps acquires high values, which reflects in an extremely large effective time increment at some integration points, leading to the convergence problems. The computational instability may be circumvented by limiting the value of viscosity computed at micro time steps by setting, e.g., $\eta_\mu \geq \eta_M^{n-1}$. This condition says that the viscosity at t_μ cannot be less than the value obtained at the last macro time step. Note that the update of viscosity at micro time steps is only relevant for the computation of $\dot{\bar{\gamma}}_{\text{p}}$, since in the elastic update of the stress state there is no actual update of the state variables controlling viscoplasticity. With the added condition the computation becomes stable, although still inaccurate, because the equivalent plastic strain rate does not account for the direction of equivalent plastic strain, but only for the absolute value of its rate. Therefore, when computing Δt_{eff}, Eq. (35), $\dot{\bar{\gamma}}_{\text{p}}$ from the compression side is added to that from the tension side, leading to an overestimated effective time increment. It is possible to introduce information on the direction of plastic deformation by multiplying $\dot{\bar{\gamma}}_{\text{p}}$ with the normalized inner product $(\boldsymbol{\sigma}_M : \boldsymbol{\sigma}_\mu / |\boldsymbol{\sigma}_M : \boldsymbol{\sigma}_\mu|)$ to define its sign, where $\boldsymbol{\sigma}_M$ is the Cauchy stress tensor computed at last converged macro time step, and $\boldsymbol{\sigma}_\mu$ is the Cauchy stress tensor computed at current micro time step. However, this action renders unstable computations and does not solve the problem, because $\dot{\bar{\gamma}}_{\text{p}}$ collected at elastic micro time steps corresponding with high compressive stress levels remains inaccurate.

The conclusion is that the introduced TH procedure is accurate as long as there is no significant reverse plasticity in the cycle. This claim is confirmed with another example on the unit cell, in which $R = -0.5$ and $\sigma^{\max}_{yy} = 100$ MPa. The TH response without

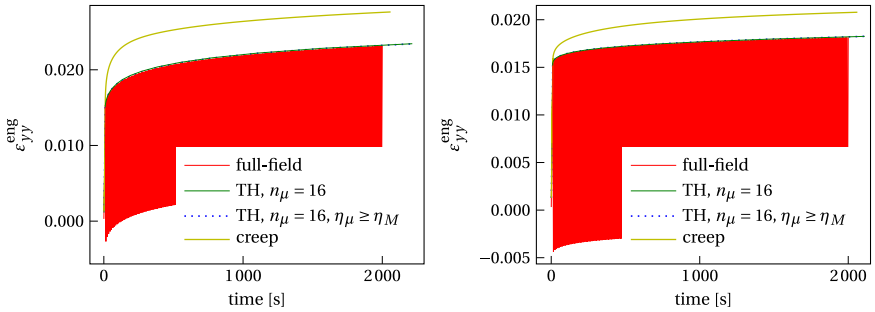

Fig. 11. Unit cell RVE under cyclic loading: $R = -0.5$, $\sigma^{\max}_{yy} = 100$ MPa, $\chi = 45°$ (left), $\chi = 90°$ (right); TH response compared with creep and full-field cyclic response; η_μ is viscosity computed at micro time steps and η_M is viscosity from last macro time step.

limiting viscosity at micro time steps and the response with limited viscosity are compared with the creep and full-field cyclic response for two loading angles: $\chi = 45°$ and $\chi = 90°$, see Fig. 11. Although the load ratio is negative, the material behavior at reversed loading is predominantly elastic with diminishing $\dot{\bar{\gamma}}_{\text{p}}$, resulting in an accurate TH prediction.

5.2. Failure prediction

Cohesive segments are now also included in the RVE, and a comparison is made with available experiments on fatigue of UD carbon/PEEK thermoplastic composites (Sundararajan, 2024). All examples assume room temperature conditions, such that $T = T_{\text{ref}}$ in Eq. (18). The fiber volume ratio is 0.4. The number of micro time steps between two macro time updates is $n_\mu = 16$, with actually running only half of them, see Section 3.2. Since the main intention here is to show the capabilities of the model, a micromodel that is too small to be entirely representative with 4 (2×2) fibers in total is considered, with a diameter of 5 μm. Similar conclusions on the mechanical behavior are expected from a bigger RVE size, especially because calibration of the cohesive model parameters was done particularly for this micromodel, improving its representativeness. Gmsh was used to generate the finite element mesh (Geuzaine and Remacle, 2009).

The model is calibrated on experimental S-t curves obtained for $R = 0.1$, $f = 1$ Hz, $\chi = 90°$ and $\chi = 45°$, see Fig. 12, where the experimental data are compared with the model results. Several things can be observed from the figure. First, the model is able to make a distinction between the plasticity controlled and crack growth controlled failure regimes. However, there is an offset in the model results from the experimental data in the transition zone between the two failure regimes for $\chi = 90°$. It should be noted that all the EGP parameters, including the relaxation spectrum, were adopted according to our previous work on creep rupture (Kovačević et al., 2024), and their calibration was not part of this work. Only the four parameters of the cohesive model were calibrated (f_n, f_{sh}, ϵ and η). While the strength parameters f_n and f_{sh} have an overall effect on the S-t (or S-N) curve, the two are also controlling the slope of the plasticity controlled part on which ϵ and η have no effect, with f_n being most dominant for the 90° loading case, while the influence of f_{sh} is stronger in the 45° case. The fatigue damage parameter ϵ largely controls the slope of the crack growth failure regime (Joosten et al., 2022), and was adopted such that the slope in $\chi = 90°$ loading is properly reproduced, see Fig. 12, where the last two points of the 90° case are considered to define the slope of the crack growth regime. Given all the inputs, the fatigue damage parameter η determines the moment when the transition between the two failure mechanisms occurs, horizontally shifting the onset of the crack growth controlled regime (Joosten et al., 2022). The value of η was adopted such that a good match was found for the last two points of the $\chi = 90°$ case, also checking for the proper transition between the failure mechanisms when $\chi = 45°$. Possibly, a further calibration of the constitutive models including the relaxation spectrum of the EGP and the cohesive model parameters could reduce the error in the results for $\chi = 90°$ and $f = 1$ Hz.

Another observation from Fig. 12 indicates a shortcoming of the model related to off-axis dependence of the crack growth controlled failure mechanism. For the carbon/PEEK composite system considered here, the same slope in S-t curves is reported for different loading angles (Sundararajan, 2024), which is in contrast with the model results, where $\chi = 45°$ features a different slope in the crack growth regime than $\chi = 90°$. Although for some composite systems a change in the slope is reported when changing off-axis angles (Pastukhov and Govaert, 2021), the reported change is in the opposite direction: lowering the off-axis angle lowers the slope of the crack growth regime.

The following example considers the RVE loaded under 90° off-axis angle. Different stress levels and frequencies are considered at the load ratio of 0.1. In Fig. 13 (left) the model prediction of the time to failure is compared with the experimental data in a *loglog* plot. The model is able to properly capture the experimentally observed frequency dependency of the two mechanisms. While the plasticity controlled part is insensitive to the loading frequency, the crack growth controlled part is frequency dependent, leading to shorter lifetimes at higher frequencies. Overall, the accuracy of the model is good, with an already discussed offset from the experiment at $f = 1$ Hz in the transition zone between two failure regimes. In Fig. 13 (right), the number of cycles to failure is plotted for different stress levels, showing a different effect of the frequency on the failure regimes. In this representation, the plasticity controlled regime shows sensitivity to the loading frequency, while the crack growth controlled part is largely independent of the loading frequency.

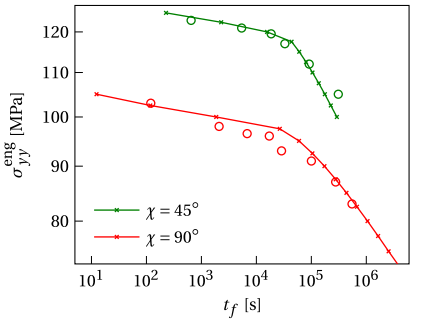

Fig. 12. Maximum stress applied versus time to failure for two off-axis angles; solid lines represent model response, with x marking stress levels considered in simulations; empty markers represent experimental data used for calibration; $R = 0.1$, $f = 1$ Hz.

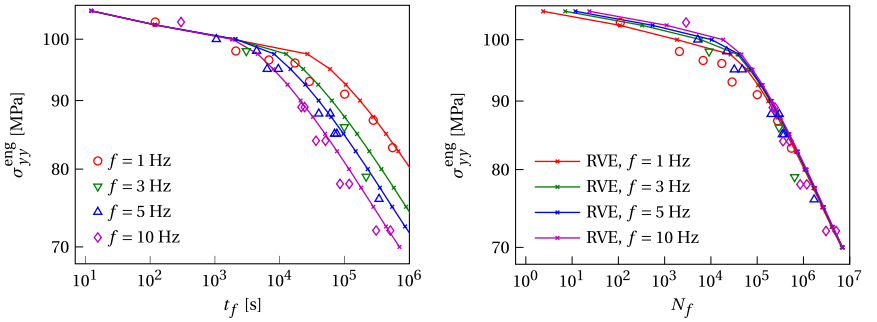

Fig. 13. Maximum stress applied versus time to failure for $\chi = 90°$, $R = 0.1$ and different frequencies (left); corresponding number of cycles to failure (right); empty markers represent experimental data, solid lines represent RVE response with x marking stresses considered in simulations.

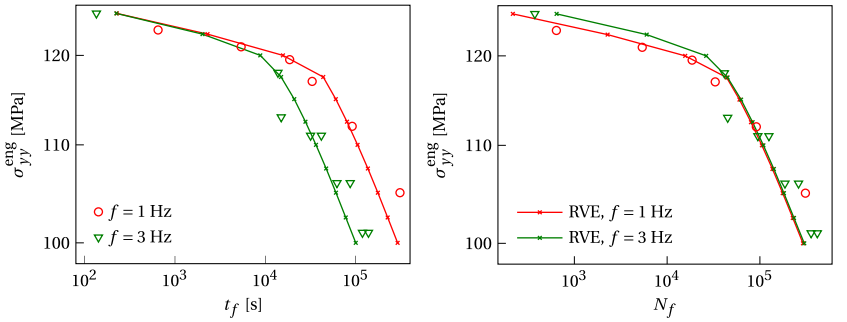

Fig. 14. Maximum stress applied versus time to failure for $\chi = 45°$, $R = 0.1$ and two different frequencies (left); corresponding number of cycles to failure (right); empty markers represent experimental response, solid lines represent model response with x marking stress levels considered in analyses.

The loading angle of 45° is considered next. The time to failure versus stress applied is plotted in Fig. 14 (left) for the load ratio $R = 0.1$ and two different frequencies in a double logarithmic plot. The model response compares satisfactorily with the experiment results, and again captures two failure mechanisms. A moderate offset from the experimental data is observed in the crack growth regime. Fig. 14 (right) illustrates the corresponding number of cycles to failure, where the conclusion regarding the frequency dependency of each failure mechanism follows that observed for $\chi = 90°$.

Another aspect in which the model may be improved is the R-dependence of the crack growth failure mechanism. In Fig. 15 the model response for $R = -0.5$ and $R = 0.2$ is compared with experimental data for $\chi = 90°$. The loading frequency is 1 Hz and 10 Hz, respectively, and the response for $R = 0.1$ is included for reference. We conclude from the figure that the trend in the number of cycles to failure with different R is captured, but the quantitative prediction is wrong. In the model, the slope of the crack growth failure mechanism is controlled by the parameter β, Eq. (57), which in turn depends on the brittleness parameter η and the relative endurance limit E, Eq. (58). In the current formulation, the parameter η has a constant value, while E is locally changing with R. This change affects the slope of the crack growth regime and shifts the cycles to failure in the correct direction. Nevertheless, the experimental data does not show a change in the slope of the crack growth controlled part for different (global) R, indicating that for the specific material system the brittleness parameter η in Eq. (58) may also be a function of R.

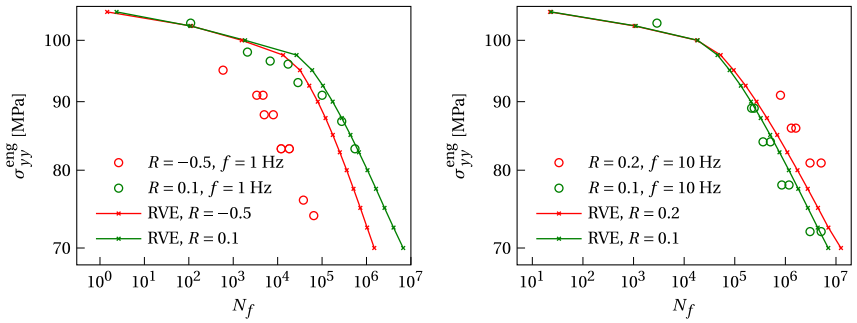

Fig. 15. Comparison of model response with experiments for $\chi = 90°$ and different load ratios: $R = -0.5$ (left), $R = 0.2$ (right); response for $R = 0.1$ included for reference; empty markers stand for experimental data; in solid lines x marks stress levels considered in simulations.

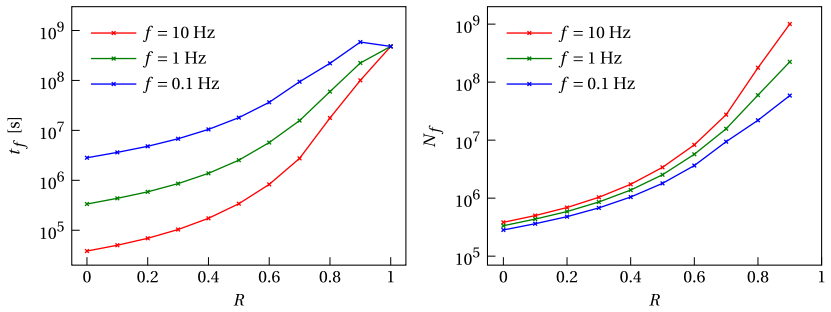

Fig. 16. Dependence of time to failure on load ratio for $\sigma_{yy}^{\max} = 85$ MPa and different frequencies predicted by the model (left); corresponding number of cycles to failure versus load ratio (right); $\chi = 90°$.

It is reported in the literature, e.g. Kanters et al. (2018), that for a stress level in the crack growth regime, the number of cycles to failure changes with frequency for different R values. Considering a different composite system Kanters et al. (2018) report an increase in the cycles to failure when increasing the frequency and the load ratio. How the model proposed here behaves in this regard is investigated next. The stress level of 85 MPa is chosen, well within the crack growth-controlled regime (cf. Fig. 13). Load ratios ranging from 0 to 1 are considered, with three different frequencies: 0.1 Hz, 1 Hz and 10 Hz. Fig. 16 (left) shows the time to failure as a function of R and f. Like in Kanters et al. (2018), for a given load ratio the time to failure increases with a decrease in the frequency. As the load ratio increases, the logarithmic difference in time to failure for different f reduces, eventually converging to a unique value for $R = 1$. The case of $R = 0.9$ and $f = 0.1$ Hz actually shows longer time to failure than the $R = 1$ case, since the material here enters the plasticity-controlled regime where low amplitude cyclic loading only prolongs the lifetime. The corresponding number of cycles to failure is plotted in Fig. 16 (right), and follows the trend reported in Kanters et al. (2018). For lower load ratios, N_f shows a small but nonzero dependence on f. For larger R values, the influence of f is much stronger as plasticity becomes more significant.

5.2.1. *Effect of viscoplasticity*

The effect of viscoplastic deformation in the matrix, which introduces the timescale to the model and correspondingly the frequency dependency in the cycles to failure, is discussed next. For $f = 1$ Hz and $R = 0.1$, simulations are repeated for the same range of stress levels, but this time assuming an elastic behavior of the matrix ($\lambda_{x,j}^{n} = 1$ in Eq. (25)). The results are compared with the model response allowing for viscoplastic deformation in the matrix, see Fig. 17 (left) for $\chi = 90°$ and Fig. 17 (right) for $\chi = 45°$. As calibrated in this study, the cohesive model combined with an elastic matrix represents quite well the crack growth failure regime for both loading angles, but does not capture the transition to plasticity controlled failure at higher stresses. Although a dedicated calibration of the cohesive model with elastic matrix could improve corresponding results at higher stresses, the adequate frequency dependence of the S-N curve would still be absent, since the number of cycles would be the quantity governing the failure process. Including viscoplastic deformation in the matrix drastically affects the model response at higher stresses for which significant yielding occurs inside the RVE and viscoplasticity practically dominates the response in this stress range. The mechanism at which the viscoplastic bulk deformation contributes to failure is the following: under the applied (creep or cyclic) stress the polymer matrix undergoes viscous deformation that increases in time. In the heterogeneous microstructure of the RVE with already initiated cohesive segments there may be a nonuniform plastic flow of the material from the two sides of the cohesive segment,

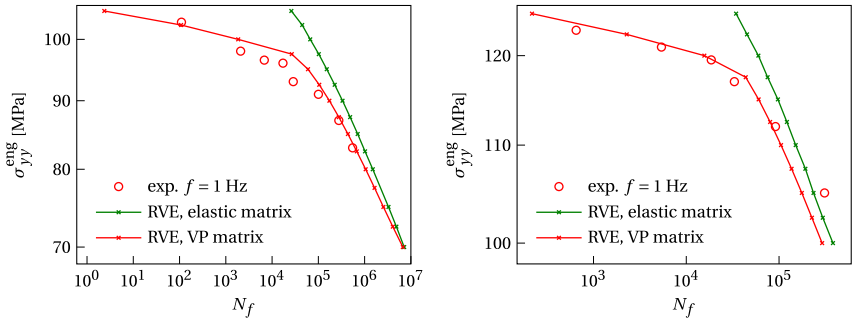

Fig. 17. Influence of viscoplastic (VP) deformation in the matrix on failure of the RVE; $\chi = 90°$ (left), $\chi = 45°$ (right), $R = 0.1$; comparison made with simulation results with elastic matrix.

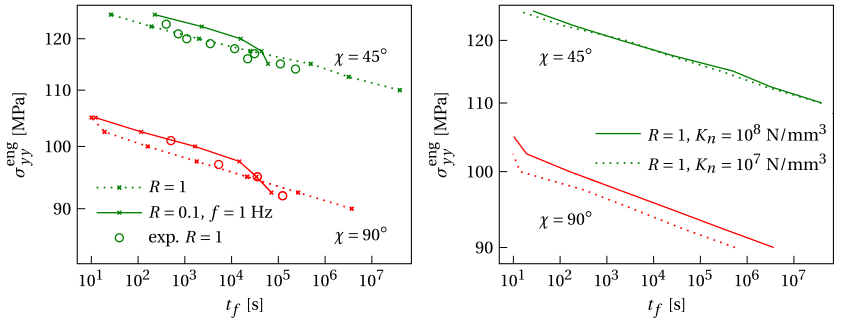

Fig. 18. RVE prediction of time to failure for different load ratios and off-axis angles, where along dotted and solid lines x marks stress levels considered in simulations; empty markers represent experimental data on creep rupture (left); influence of dummy stiffness on time to failure in creep loading for two off-axis angles (right).

leading to an opening of the cohesive zone and activating the quasi-static damage variable.[1] It is known in the polymer literature that crack propagation in cyclic loading features a static (creep) component and a cyclic component (Dumpleton and Bucknall, 1987; Hu et al., 2003). As for physical interpretation, the cyclic component of crack propagation is due to bending, buckling or crushing fibrils (Zhou and Brown, 1992), and is represented with the fatigue damage variable in the model. On the other hand, the creep component relates to failure of the fibrils in the fracture process zone (or craze zone) due to disentanglement or chain scission (Zhou et al., 2011). In the present model, it becomes dominant at higher stresses applied on the RVE, as opposed to the cyclic component that is dominant at lower applied stresses. Finally, the small but nonzero influence on the lifetime that is found from viscoplasticity in the crack growth regime mirrors the small frequency dependence that was found for the number of cycles to failure for low R-values in Fig. 16. Both observations point at a small but non-negligible influence of time-dependent plasticity on the lifetime in high-cycle fatigue.

5.2.2. Creep rupture

In order to elucidate the role of the loading amplitude on the time to failure in the plasticity controlled regime, the model response for $R = 1$ (creep) is compared with the model response for $R = 0.1$ and $f = 1$ Hz, see Fig. 18 (left), where the experimental results for creep rupture are also included (Sundararajan, 2024). Note that for $R = 1$, there is no micro time stepping in the simulations. As observed from the figure, the model predicts well the time to failure in creep, which shifts to shorter timescales as compared to the plasticity controlled regime in cyclic loading. This shift is due to the faster viscous deformation in the bulk material under a constant loading than that under cyclic loading. Despite this difference, both cases feature the same slope in the S-t curve, indicating the same failure kinetics. It is worth noting that the present model better predicts creep rupture than the model we introduced in Kovačević et al. (2024). There, a general cohesive initiation criterion based on the critical energy stored in the bulk material was considered, that further required the presence of another failure mechanism on the cohesive surface, to speed up the failure process for different loading angles. That approach led to a lower predictive accuracy compared to the current results. However, the described mechanism to activate the quasi-static damage in the current model is not possible in a homogeneous material like neat polymer, where the uniform viscous deformation of the surrounding bulk material will not change the cohesive zone opening, and the quasi-static damage variable will never be activated. In such a scenario, the modeling of creep rupture or plasticity controlled failure in fatigue

[1] Yet another mechanism at which the quasi-static damage variable can be activated in the present context is the application of the engineering stress, which means that in tension the actual stress on the RVE is increasing with deformation, Eq. (8).

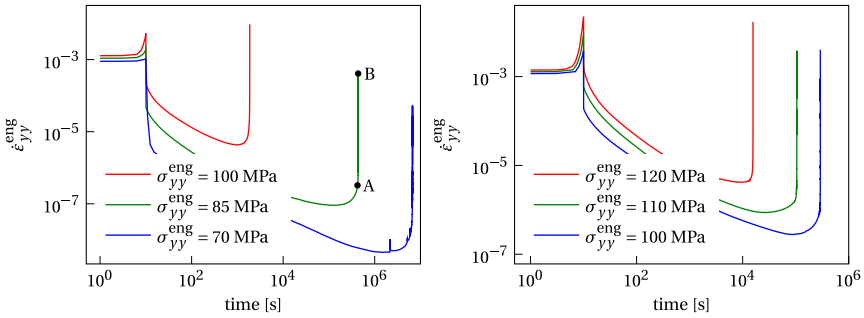

Fig. 19. Homogenized strain rate versus time computed at macro time steps for different maximum stress levels, $f = 1$ Hz, $\chi = 90°$ (left) and $\chi = 45°$ (right); failure of RVE coincides with abrupt increase in strain rate; 153 macro time steps needed to reach point A ($t = 4.217 \cdot 10^5$ s) and 1008 macro time steps needed to reach point B ($t = 4.357 \cdot 10^5$ s).

requires the existence of another failure mechanism if the cohesive zone approach is followed, e.g., viscous degradation on the cohesive surface (Kovačević et al., 2024).

Another important aspect about the model is that the cohesive model dummy stiffness K_n affects the model response. An indication for this is found in the observation that early initiation of cracks (using the endurance limit at $R = 0.1$) is essential to obtain failure in creep loading that is within the timescale of experimental data, even though the *fatigue damage* remains inactive for $R = 1$. To support this claim, the RVE is again exposed to a constant load, $R = 1$, with the dummy stiffness reduced from 10^8 N/mm^3 to 10^7 N/mm^3. The corresponding time to failure curves are shown in Fig. 18 (right), for two off-axis angles. It follows from the figure that for $\chi = 45°$ the response is almost unaltered by the change in stiffness. Nevertheless, the $\chi = 90°$ case shows a significant shift in the lifetime when changing the dummy stiffness. By lowering the value of K_n, it becomes easier for the two sides of the cohesive segment to detach, increasing the effect of viscoplastic flow in the surrounding matrix.

Although not every mechanism is fully captured, the proposed model shows a very good ability to reproduce highly-complex failure behavior.

5.2.3. Failure state of the RVE

A failure state of the RVE is reached by propagating microcracks through the matrix. The RVE is considered to have failed when the adaptive stepping algorithm cannot find a converging time increment anymore. It is checked from looking at the homogenized strain rates whether this non-convergence is preceded by increased deformation rates, as can be expected to happen just before the material cannot carry the applied load anymore. The homogenized strain rate is computed at macro time steps, when the applied stress is at its maximum. Fig. 19 illustrates the evolution of the strain rate for $\chi = 90°$ and $\chi = 45°$, $R = 0.1$, $f = 1$ Hz and different stress levels. After the initial loading phase is over ($t = 10$ s) and the cycling has started, the homogenized strain rate gradually decreases. Subsequently, the strain rate reaches a minimum value after which it transitions to an abruptly increasing phase. It is clear that the non-convergence of the model, that is taken as failure of the material, is caused by instability in the homogenized material response. A similar evolution of the strain rate is observed experimentally for creep loading, see e.g. Erartsin et al. (2022).

For some loading cases, capturing the equilibrium path after the minimum strain rate is passed, may be computationally demanding. In Fig. 19 (left), points A and B are indicated for the stress level of 85 MPa, both of which belong to the phase of quickly increasing strain rate. The number of macro time steps needed to reach the point A ($t = 4.217 \cdot 10^5$ s, $runtime = 4.66 \cdot 10^4$ s) is 153, while the point B ($t = 4.357 \cdot 10^5$ s, $runtime = 9.776 \cdot 10^4$ s) was reached after 1008 macro time steps. Also, in some loading cases including the considered one, transition from point A to point B is not monotonic, i.e., the strain rate value oscillates, with the overall trend to increase. Furthermore, it is possible to lose convergence at micro time steps in this last phase of the simulation. In such a case, the data collected from the last successful micro time stepping are used to compute Δt_{eff} at macro time steps. This is the reason why the runtime between the points A and B differs by a factor of 2, while the number of macro time steps differs by a factor of 7, approximately. The clear increase in strain rate that is consistently found in the final phase of the simulation indicates that the non-convergence with which the simulation ends is indeed caused by the material losing the ability to carry the prescribed load.

Deformed RVEs at the moment of failure are shown in the contour plots of Fig. 20, where the distribution of the equivalent plastic strain is illustrated together with cohesive microcracks for two loading angles. Although it features much less equivalent plastic strain than the 45° example, the 90° case does not lack yielding in the matrix, which brings it to the plasticity controlled failure regime, see Fig. 17. The difference in $\bar{\gamma}_{\text{p}}$ for two loading angles is due to the difference in shear deformation, which, by definition, promotes the accumulation of the plastic strain in the EGP model. In Fig. 20 (right) the discretization and the crack pattern are visualized, where the thicker lines indicate initiated cohesive segments in one typical simulation. In the depicted example, except for two cohesive segments (encircled green lines) in the elastic/unloading phase, all other cohesive segments (black lines) are in the loading phase, i.e., the damage increases at the moment of failure.

When changing the mode of failure, the density of developing cohesive microcracks in the domain changes as well. This fact is illustrated in Fig. 21, where the network of cohesive microcracks is shown for $\chi = 90°$ and three stress levels at the moment of

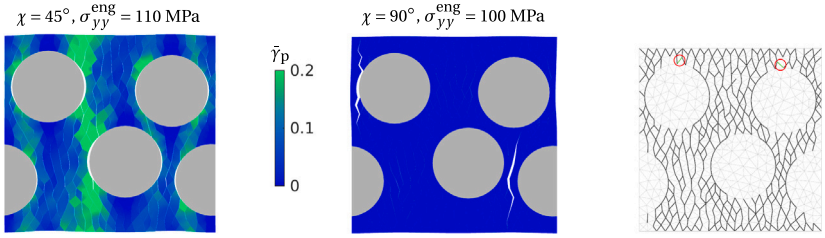

Fig. 20. Front view of 3D thin slice RVE showing equivalent plastic strain and cohesive microcracks in the matrix at the moment of failure for two loading angles, $R = 0.1$ and $f = 1$ Hz; gray lines indicating finite element mesh, with thicker lines representing initiated cohesive segments for typical simulation (right); black lines indicate damaging cohesive segments, while (encircled) green lines represent cohesive segments in elastic/unloading phase.

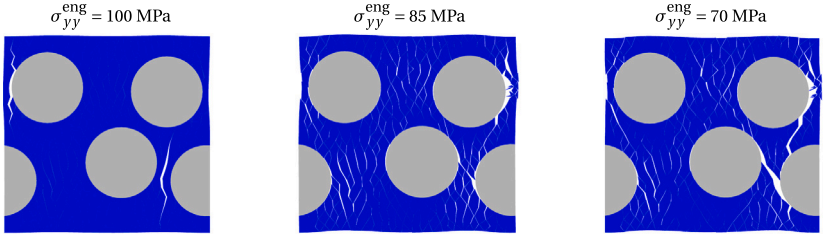

Fig. 21. Density of developing cohesive microcracks at failure for $\chi = 90°$, $R = 0.1$, $f = 1$ Hz and three stress levels; 100 MPa belongs to plasticity controlled failure regime; the other two are in crack growth failure regime, see Fig. 13.

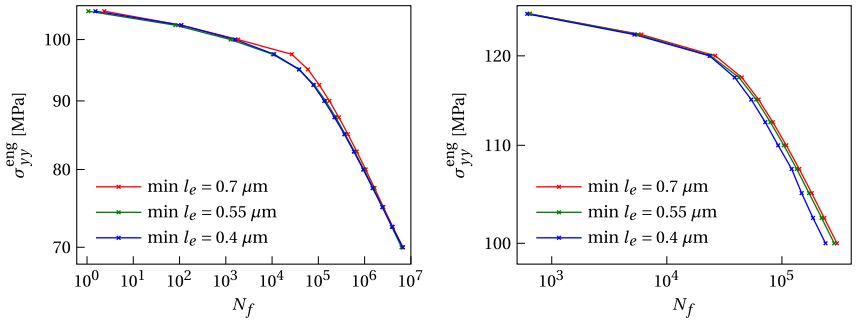

Fig. 22. RVE prediction of S-N curves for different mesh sizes defined by minimum length of finite element; $\chi = 90°$, $f = 1$ Hz (left); $\chi = 45°$, $f = 3$ Hz (right); $R = 0.1$.

failure. In the plasticity controlled regime, $\sigma_{yy}^{max} = 100$ MPa, two dominant cohesive cracks are running through the RVE. As the applied stress decreases and the failure mode transitions to the brittle mechanism, the density of developing cohesive microcracks increases.

5.2.4. Mesh dependency

Finally, S-N curves are generated with three different mesh sizes, see Fig. 22 (left) for $\chi = 90°$ and Fig. 22 (right) for $\chi = 45°$, where the mesh size is defined by the minimum finite element length. While for $\chi = 90°$ refinement of the mesh leads to a similar model response, for $\chi = 45°$ the results indicate a significant dependence on the mesh density. In this regard, careful studies on mesh dependency of the model are needed, particularly on the objectivity of viscosity evolution in the EGP model, and the influence of inter-element crack patterns on the model response.

6. Conclusion

In this work, a microscale spatial and two-scale temporal framework is introduced to capture the time- and cycle dependency of failure in unidirectional composites under cyclic loading. To efficiently pass through the loading signal, an adaptive stepping scheme is proposed. The scheme consists of macro time steps where viscoplasticity evolves in the polymer matrix, and micro time steps with an elastic update in the bulk material models, and blocked cohesive initiation and damage evolution in the cohesive zone model. The response of the matrix in cyclic loading is represented with the Eindhoven Glassy Polymer material model, for which a version based on two time scales is formulated. Following principles of the time homogenization procedure, an effective time increment is

computed for integration points representing the matrix, and used in macro time step updates. The carbon fiber reinforcement is represented with a hyperelastic transversely isotropic material model. For considered examples, the time homogenization approach is shown to accurately capture the cyclic evolution of viscoplastic deformations for a range of stress ratios from $R = -0.5$ to $R = 1$. Only for lower negative R-values, when reverse plasticity becomes significant, the proposed approach loses accuracy.

Failure of the RVE is achieved by propagation of microcracks through the domain, whereby microcracking is represented with Dávila's cycle-dependent cohesive model, combined with an endurance limit-based cohesive initiation criterion. Eventually, the time-dependent failure process features two components. Firstly, there is cyclic failure due to the buckling and crushing of fibrils in the process zone, represented with the fatigue damage in the cohesive model. Secondly, there is nonuniform viscoplastic flow in the bulk material around cohesive segments, which may trigger quasi-static damage of the cohesive model. The static (creep) component is dominant at higher applied stresses, as opposed to the cyclic (fatigue) component, which dominates the response at lower stresses.

The model performance is compared with available experiments on fatigue of UD carbon/PEEK thermoplastic composites, tested under different off-axis angles, load ratios and frequencies. The model is able to capture the transition from plasticity controlled to crack growth controlled failure, and properly captures the frequency dependency of each mechanism. Despite showing very good performance for the aforementioned cases, the R-dependence and the off-axis angle dependence of the number of cycles to failure in the crack growth controlled regime is still not captured well. For the studied material system, modification of the cohesive zone model will be required to achieve a model that can make accurate predictions for a wider range of load cases.

As a limit case when $R = 1$, the model is able to capture the failure kinetics in creep loading, which are the same as in the plasticity controlled regime under cyclic loading. The difference is that the creep rupture state shifts toward shorter lifetimes due to the faster viscoplastic deformation under a constant loading. Regarding the accuracy of the predicted time to failure, the model proposed here outperforms our earlier model specifically developed for creep rupture (Kovačević et al., 2024). A notable difference is that here we use a different initiation criterion that allows for early initiation of many cohesive segments. The heterogeneity of the microstructure allows for nonuniform viscoplastic flow of the matrix around cohesive segments, which triggers quasi-static damage and leads to creep rupture. However, this mechanism is not possible in neat polymer, where the matrix uniformly flows around cohesive segments and quasi-static damage does not evolve. In such a scenario, another failure mechanism is required to trigger the failure process, e.g., viscous degradation on the cohesive surface (Kovačević et al., 2024).

CRediT authorship contribution statement

D. Kovačević: Writing – original draft, Visualization, Software, Methodology, Investigation, Conceptualization. **P. Hofman:** Writing – review & editing, Software, Methodology, Conceptualization. **I.B.C.M. Rocha:** Writing – review & editing, Software, Methodology, Conceptualization. **F.P. van der Meer:** Writing – review & editing, Supervision, Software, Methodology, Funding acquisition, Conceptualization.

Declaration of competing interest

The authors declare that they have no known competing financial interests or personal relationships that could have appeared to influence the work reported in this paper.

Acknowledgment

This research forms part of the research programme of DPI, project #811t17.

Appendix

All parameters of constitutive models considered in this paper are listed in Table A.6. An explanation is provided on how these parameters can be obtained, and necessary experiments are indicated. Given the large number of parameters governing the constitutive models, the outlined procedure to determine their values is not unique, but represent one possible way to obtain these values.

Regarding the (two-scale) EGP model representing the polymer matrix, the bulk modulus κ can be obtained from a uniaxial test of neat polymer, whereby the Young's modulus and the Poisson's ratio are determined and used to compute the bulk modulus. To ensure a homogeneous deformation of the testing sample, compression is preferred over tension. The hardening modulus G_r can be obtained from a stress–strain curve in uniaxial compression, as a slope of the curve at large strains (Klompen et al., 2005). The activation volume V_x ($x = \alpha, \beta$) is obtained by fitting the slope of the yield stress plotted versus strain rate in a semi-log scale (Van Breemen et al., 2011). Hence, a series of experiments in uniaxial compression at different strain rates (e.g. $10^{-5} - 10^{-2}$/s) is necessary. If present, a change in the slope of the plotted curve would indicate the presence of another relaxation process ($V_\beta \neq 0$). The activation enthalpy ΔH_x is determined from multiple experiments in uniaxial compression at different temperatures (e.g. 20° – 100° C), where ΔH_x is calibrated to match the observed yield stress for different temperatures. Again, if a change in the slope of this curve is observed, it means that another relaxation process also contributes to the material response in the given temperature range ($\Delta H_\beta \neq 0$). The relaxation spectrum ($G_{x,j}$ and $\eta_{0x,j}$) is determined from one uniaxial test considering the pre-yield response as explained in Van Breemen et al. (2011). The reader should note that an alternative exists in calibrating Eyring parameters (activation

Table A.6
Parameters of constitutive models used in the paper.

Eindhoven Glassy Polymer model (matrix)	
κ	Bulk modulus
G_r	Hardening modulus
V_x	Activation volume
ΔH_x	Activation enthalpy
$G_{x,j}$	Shear moduli
$\eta_{0x,j}$	Initial viscosities
μ_x	Pressure dependency
S_x	State parameter
Transversely isotropic model (fibers)	
E_1	Young's modulus in preferential stiffness direction
E_2	Young's modulus in the plane of isotropy
G_{12}	shear modulus in planes perpendicular to the isotropic plane
ν_{12}	Poisson's ratio in planes perpendicular to the isotropic plane
ν_{23}	Poisson's ratio in the plane of isotropy
Dávila's cohesive zone model (cracks)	
K_n	Dummy stiffness in normal direction
G_{Ic}	Mode I fracture energy
G_{IIc}	Mode II fracture energy
f_n	Quasi-static strength in normal direction
f_{sh}	Quasi-static strength in shear direction
η_{BK}	Interaction parameter
ϵ	Relative endurance limit at $R = -1$
η	Brittleness parameter
p	Fitting parameter

volume, activation enthalpy, initial viscosities), if these parameters are modeled as deformation dependent (Sundararajan, 2024), which is not the case in this study. The pressure dependency parameter μ_x is obtained by fitting the yield stress for different values of imposed hydrostatic pressure (Klompen et al., 2005). Finally, the state parameter $S_x = S_{\mathrm{a}x} \cdot R_{\gamma x}$ (see Section 3.1) can be determined from one uniaxial compression test (Klompen et al., 2005), and will be nonzero if there is an intrinsic strain-softening of the material. In this study, it is set to zero, see Section 3.1.

Given a different crystallinity of neat polymer (PEEK) and the fiber reinforced polymer, a direct application of this set of parameters would result in an inaccurate prediction of the composite stress–strain response under different loading conditions (Sundararajan, 2024). Therefore, a modification of the initial set of parameters is needed to improve the simulation accuracy. For example, the relaxation spectrum can be shifted until a satisfactory accuracy is reached. Until a systematic relationship between the change in material crystallinity and the change in the material properties is established, this shift can be done by trial and error.

As for the transversely isotropic material model representing carbon fibers, the Young's modulus in the preferential stiffness direction is obtained from quasi-static experiments on UD material in longitudinal direction. Experimental procedures to obtain other parameters for the material model are more involved, so their values were in this work adopted from literature. The Young's modulus E_2 and the Poisson's ratio ν_{23} were adopted according to Miyagawa et al. (2005). The shear modulus G_{12} was fitted to match the strain-time response under $\chi = 45°$ creep loading (Kovačević et al., 2024). The Poisson's ratio $\nu_{12} = 0.05$ was adopted from Kovačević and Van der Meer (2022), the value of which also ensures the computational stability of the material model.

Finally, the parameters of the cohesive model need to be determined. The value of the dummy stiffness K_n needs to be high enough to prevent spurious effects on the homogenized strain of the micromodel in the presence of many cohesive segments, but low enough to not cause numerical difficulties. Fracture energies and the quasi-static strength parameters can be obtained from quasi-static experiments on UD material under 90° and 45°, where fitting the stress at failure and the strain at failure for two loading angles is enough information to determine these four parameters. In the present study, fracture energies G_{Ic} and G_{IIc} were adopted from Kovačević et al. (2022), while the quasi-static strength parameters f_n and f_{sh} were determined to fit the slope of S-t curves in plasticity controlled failure under $\chi = 90°$, $\chi = 45°$ and $f = 1$ Hz. The interaction parameter η_{BK} can be determined from mixed-mode bending tests (Benzeggagh and Kenane, 1996). The fitting parameter p can be adopted from literature, e.g. Raimondo et al. (2022), where different values have been considered for p. The brittleness parameter η is determined such that the transition from plasticity controlled failure to crack growth controlled failure is captured. The parameter ϵ is fitted such that the slope of the crack growth controlled regime is accurately represented.

Data availability

Data presented in this article are available at the 4TU.ResearchData repository through https://doi.org/10.4121/c9592e56-9284-42ba-92b3-b6448e5beddb.

References

Arteiro, A., Catalanotti, G., Melro, A.R., Linde, P., Camanho, P.P., 2014. Micro-mechanical analysis of the in situ effect in polymer composite laminates. Compos. Struct. 116, 827–840. http://dx.doi.org/10.1016/j.compstruct.2014.06.014.

Benzeggagh, M., Kenane, M., 1996. Measurement of mixed-mode delamination fracture toughness of unidirectional glass/epoxy composites with mixed-mode bending apparatus. Compos. Sci. Technol. 56 (4), 439–449. http://dx.doi.org/10.1016/0266-3538(96)00005-X.

Bonet, J., Burton, A.J., 1998. A simple orthotropic, transversely isotropic hyperelastic constitutive equation for large strain computations. Comput. Methods Appl. Mech. Engrg. 162 (1), 151–164. http://dx.doi.org/10.1016/S0045-7825(97)00339-3.

Camacho, G.T., Ortiz, M., 1996. Computational modelling of impact damage in Brittle materials. Int. J. Solids Struct. 33 (20), 2899–2938. http://dx.doi.org/10.1016/0020-7683(95)00255-3.

Crouch, R., Oskay, C., Clay, S., 2013. Multiple spatio-temporal scale modeling of composites subjected to cyclic loading. Comput. Mech. 51 (1), 93–107. http://dx.doi.org/10.1007/s00466-012-0707-9.

Dávila, C.G., 2020. From S-N to the Paris law with a new mixed-mode cohesive fatigue model for delamination in composites. Theor. Appl. Fract. Mech. 106, 102499. http://dx.doi.org/10.1016/j.tafmec.2020.102499.

Dumpleton, P., Bucknall, C., 1987. Comparison of static and dynamic fatigue crack growth rates in high-density polyethylene. Int. J. Fatigue 9 (3), 151–155. http://dx.doi.org/10.1016/0142-1123(87)90070-3.

Erartsin, O., Amiri-Rad, A., Van Drongelen, M., Govaert, L.E., 2022. Time-dependent failure of off-axis loaded unidirectional glass/iPP composites. J. Appl. Polym. Sci. 139 (23), 52293. http://dx.doi.org/10.1002/app.52293.

Eyring, H., 1936. Viscosity, plasticity, and diffusion as examples of absolute reaction rates. J. Chem. Phys. 4 (4), 283–291. http://dx.doi.org/10.1063/1.1749836.

Fish, J., Yu, Q., 2002. Computational mechanics of fatigue and life predictions for composite materials and structures. Comput. Methods Appl. Mech. Engrg. 191 (43), 4827–4849. http://dx.doi.org/10.1016/S0045-7825(02)00401-2.

Geuzaine, C., Remacle, J.-F., 2009. Gmsh: A 3-D finite element mesh generator with built-in pre- and post-processing facilities. Internat. J. Numer. Methods Engrg. 79 (11), 1309–1331. http://dx.doi.org/10.1002/nme.2579.

Haouala, S., Doghri, I., 2015. Modeling and algorithms for two-scale time homogenization of viscoelastic-viscoplastic solids under large numbers of cycles. Int. J. Plast. 70, 98–125. http://dx.doi.org/10.1016/j.ijplas.2015.03.005.

Hessman, P.A., Welschinger, F., Hornberger, K., Böhlke, T., 2023. A micromechanical cyclic damage model for high cycle fatigue failure of short fiber reinforced composites. Composites B 264, 110855. http://dx.doi.org/10.1016/j.compositesb.2023.110855.

Hille, T.S., Suiker, A.S.J., Turteltaub, S., 2009. Microcrack nucleation in thermal barrier coating systems. Eng. Fract. Mech. 76 (6), 813–825. http://dx.doi.org/10.1016/j.engfracmech.2008.12.010.

Hofman, P., Van der Meer, F.P., Sluys, L.J., 2024. A numerical framework for simulating progressive failure in composite laminates under high-cycle fatigue loading. Eng. Fract. Mech. 295, 109786. http://dx.doi.org/10.1016/j.engfracmech.2023.109786.

Hu, Y., Summers, J., Hiltner, A., Baer, E., 2003. Correlation of fatigue and creep crack growth in poly(vinyl chloride). J. Mater. Sci. 38, 633–642.

Janssen, R.P.M., De Kanter, D., Govaert, L.E., Meijer, H.E.H., 2008a. Fatigue life predictions for glassy polymers: a constitutive approach. Macromolecules 41 (7), 2520–2530. http://dx.doi.org/10.1021/ma071273i.

Janssen, R.P.M., Govaert, L.E., Meijer, H.E.H., 2008b. An analytical method to predict fatigue life of thermoplastics in uniaxial loading: sensitivity to wave type, frequency, and stress amplitude. Macromolecules 41 (7), 2531–2540. http://dx.doi.org/10.1021/ma071274a.

Joosten, M.W., Dávila, C.G., Yang, Q., 2022. Predicting fatigue damage in composites subjected to general loading conditions. Composites A 156, 106862. http://dx.doi.org/10.1016/j.compositesa.2022.106862.

Juvinall, R.C., Marshek, K.M., 2020. Fundamentals Of Machine Component Design. John Wiley & Sons.

Kanters, M.J.W., Engels, T.A.P., Van Erp, T.B., Govaert, L.E., 2018. Predicting long-term crack growth dominated static fatigue based on short-term cyclic testing. Int. J. Fatigue 112, 318–327. http://dx.doi.org/10.1016/j.ijfatigue.2018.03.011.

Kanters, M.J.W., Kurokawa, T., Govaert, L.E., 2016. Competition between plasticity-controlled and crack-growth controlled failure in static and cyclic fatigue of thermoplastic polymer systems. Polym. Test. 50, 101–110. http://dx.doi.org/10.1016/j.polymertesting.2016.01.008.

Ke, L., Van der Meer, F.P., 2022. A computational homogenization framework with enhanced localization criterion for macroscopic cohesive failure in heterogeneous materials. J. Theor. Comput. Appl. Mech. http://dx.doi.org/10.46298/jtcam.7707.

Khaleghi, H., Amiri-Rad, A., Mashayekhi, M., 2022. A thermodynamically consistent continuum damage model for time-dependent failure of thermoplastic polymers. Int. J. Plast. 154, 103278. http://dx.doi.org/10.1016/j.ijplas.2022.103278.

Klompen, E.T.J., Engels, T.A.P., Govaert, L.E., Meijer, H.E.H., 2005. Modeling of the postyield response of glassy polymers: influence of thermomechanical history. Macromolecules 38 (16), 6997–7008. http://dx.doi.org/10.1021/ma050498v.

Klompen, E., Govaert, L., 1999. Nonlinear viscoelastic behaviour of thermorheologically complex materials. Mech. Time Depend Mater. 3 (1), 49–69. http://dx.doi.org/10.1023/A:1009853024441.

Kovačević, D., Sundararajan, B.K., Van der Meer, F.P., 2022. Microscale modeling of rate-dependent failure in thermoplastic composites under off-axis loading. Eng. Fract. Mech. 276, 108884. http://dx.doi.org/10.1016/j.engfracmech.2022.108884.

Kovačević, D., Sundararajan, B.K., Van Der Meer, F.P., 2024. Micromechanical model for off-axis creep rupture in unidirectional composites undergoing finite strains. Composites A 176, 107860. http://dx.doi.org/10.1016/j.compositesa.2023.107860.

Kovačević, D., Van der Meer, F.P., 2022. Strain-rate based arclength model for nonlinear microscale analysis of unidirectional composites under off-axis loading. Int. J. Solids Struct. 250, 111697. http://dx.doi.org/10.1016/j.ijsolstr.2022.111697.

Melro, A.R., Camanho, P.P., Pinho, S.T., 2012. Influence of geometrical parameters on the elastic response of unidirectional composite materials. Compos. Struct. 94 (11), 3223–3231. http://dx.doi.org/10.1016/j.compstruct.2012.05.004.

Miyagawa, H., Sato, C., Mase, T., Drown, E., Drzal, L.T., Ikegami, K., 2005. Transverse elastic modulus of carbon fibers measured by Raman spectroscopy. International Conference on Recent Advances in Composite Materials, Mater. Sci. Eng. A International Conference on Recent Advances in Composite Materials, 412 (1), 88–92.http://dx.doi.org/10.1016/j.msea.2005.08.037,

Mohammadi, B., Shokrieh, M.M., Jamali, M., Mahmoudi, A., Fazlali, B., 2021. Damage-entropy model for fatigue life evaluation of off-axis unidirectional composites. Compos. Struct. 270, 114100. http://dx.doi.org/10.1016/j.compstruct.2021.114100.

Nguyen-Thanh, C., Nguyen, V.P., De Vaucorbeil, A., Kanti Mandal, T., Wu, J.-Y., 2020. Jive: An open source, research-oriented C++ library for solving partial differential equations. Adv. Eng. Softw. 150, 102925. http://dx.doi.org/10.1016/j.advengsoft.2020.102925.

Ni, T., Zaccariotto, M., Galvanetto, U., 2023. A peridynamic approach to simulating fatigue crack propagation in composite materials. Proc. R. Soc. A 381 (2240), 20210217. http://dx.doi.org/10.1098/rsta.2021.0217.

Oskay, C., Fish, J., 2004. Fatigue life prediction using 2-scale temporal asymptotic homogenization. Internat. J. Numer. Methods Engrg. 61 (3), 329–359. http://dx.doi.org/10.1002/nme.1069.

Pastukhov, L.V., Govaert, L.E., 2021. Crack-growth controlled failure of short fibre reinforced thermoplastics: influence of fibre orientation. Int. J. Fatigue 143, 105982. http://dx.doi.org/10.1016/j.ijfatigue.2020.105982.

Raimondo, A., Dávila, C.G., Bisagni, C., 2022. Cohesive analysis of a 3D benchmark for delamination growth under quasi-static and fatigue loading conditions. Fatigue Fract. Eng. Mater. Struct. 45 (7), 1942–1952. http://dx.doi.org/10.1111/ffe.13712.

Reifsnider, K.L., Gao, Z., 1991. A micromechanics model for composites under fatigue loading. Int. J. Fatigue 13 (2), 149–156. http://dx.doi.org/10.1016/0142-1123(91)90007-L.

Rocha, I., Raijmaekers, S., Van Der Meer, F., Nijssen, R., Fischer, H., Sluys, L., 2017. Combined experimental/numerical investigation of directional moisture diffusion in glass/epoxy composites. Compos. Sci. Technol. 151, 16–24. http://dx.doi.org/10.1016/j.compscitech.2017.08.002.

Rocha, I.B.C.M., Van der Meer, F.P., Sluys, L.J., 2019. Efficient micromechanical analysis of fiber-reinforced composites subjected to cyclic loading through time homogenization and reduced-order modeling. Comput. Methods Appl. Mech. Engrg. 345, 644–670. http://dx.doi.org/10.1016/j.cma.2018.11.014.

Senden, D.J.A., Krop, S., Van Dommelen, J.A.W., Govaert, L.E., 2012. Rate- and temperature-dependent strain hardening of polycarbonate. J. Polym. Sci. B 50 (24), 1680–1693. http://dx.doi.org/10.1002/polb.23165.

Sundararajan, B.K., 2024. Matrix Dominated Failure in Continuous Carbon Fibre Reinforced Poly(Ether Ether Ketone). (Ph.D. thesis). University of Twente, Enschede, The Netherlands, http://dx.doi.org/10.3990/1.9789036560405.

Tervoort, T.A., Smit, R.J.M., Brekelmans, W.A.M., Govaert, L.E., 1997. A constitutive equation for the elasto-viscoplastic deformation of glassy polymers. Mech. Time Depend Mater. 1 (3), 269–291. http://dx.doi.org/10.1023/A:1009720708029.

Totry, E., González, C., LLorca, J., 2008. Failure locus of fiber-reinforced composites under transverse compression and out-of-plane shear. Compos. Sci. Technol. 68 (3), 829–839. http://dx.doi.org/10.1016/j.compscitech.2007.08.023.

Turon, A., Camanho, P.P., Costa, J., Dávila, C.G., 2006. A damage model for the simulation of delamination in advanced composites under variable-mode loading. Mech. Mater. 38 (11), 1072–1089. http://dx.doi.org/10.1016/j.mechmat.2005.10.003.

Turon, A., González, E.V., Sarrado, C., Guillamet, G., Maimí, P., 2018. Accurate simulation of delamination under mixed-mode loading using a cohesive model with a mode-dependent penalty stiffness. Compos. Struct. 184, 506–511. http://dx.doi.org/10.1016/j.compstruct.2017.10.017.

Van Breemen, L.C.A., Klompen, E.T.J., Govaert, L.E., Meijer, H.E.H., 2011. Extending the EGP constitutive model for polymer glasses to multiple relaxation times. J. Mech. Phys. Solids 59 (10), 2191–2207. http://dx.doi.org/10.1016/j.jmps.2011.05.001.

Van der Meer, F.P., 2012. Mesolevel modeling of failure in composite laminates: constitutive, kinematic and algorithmic aspects. Arch. Comput. Methods Eng. 19 (3), 381–425. http://dx.doi.org/10.1007/s11831-012-9076-y.

Van der Meer, F.P., 2016. Micromechanical validation of a mesomodel for plasticity in composites. Eur. J. Mech. A Solids 60, 58–69. http://dx.doi.org/10.1016/j.euromechsol.2016.06.008.

Van der Meer, F.P., Sluys, L.J., 2009. A phantom node formulation with mixed mode cohesive law for splitting in laminates. Int. J. Fract. 158 (2), 107. http://dx.doi.org/10.1007/s10704-009-9344-5.

Verhoosel, C.V., Remmers, J.J.C., Gutiérrez, M.A., 2009. A dissipation-based arc-length method for robust simulation of brittle and ductile failure. Internat. J. Numer. Methods Engrg. 77 (9), 1290–1321. http://dx.doi.org/10.1002/nme.2447.

Yu, Q., Fish, J., 2002. Temporal homogenization of viscoelastic and viscoplastic solids subjected to locally periodic loading. Comput. Mech. 29 (3), 199–211. http://dx.doi.org/10.1007/s00466-002-0334-y.

Zhou, Y.-Q., Brown, N., 1992. The mechanism of fatigue failure in a polyethylene copolymer. J. Polym. Sci. B 30 (5), 477–487. http://dx.doi.org/10.1002/polb.1992.090300507.

Zhou, Z., Hiltner, A., Baer, E., 2011. Predicting long-term creep failure of bimodal polyethylene pipe from short-term fatigue tests. J. Mater. Sci. 46 (1), 174–182. http://dx.doi.org/10.1007/s10853-010-4902-9.